

Interacting bosons on crystalline and quasiperiodic ladders in a magnetic field

Dean Johnstone^{1,2,*}, Patrik Öhberg,¹ and Callum W. Duncan³

¹*SUPA, Institute of Photonics and Quantum Sciences, Heriot-Watt University, Edinburgh EH14 4AS, United Kingdom*

²*CPHT, CNRS, École polytechnique, Institut Polytechnique de Paris, 91120 Palaiseau, France*

³*Department of Physics, SUPA and University of Strathclyde, Glasgow G4 0NG, United Kingdom*



(Received 11 January 2023; revised 5 April 2023; accepted 9 May 2023; published 27 June 2023)

We study a variety of Hofstadter ladders in order to probe the interplay between interactions, an applied magnetic field, and crystalline or quasiperiodic geometries. Motion will be induced on charged particles when a magnetic field is present, which can result in exotic distributions of current on a lattice. Typically, the geometry of a ladder lattice is assumed to be homogeneous. In this paper, however, we will study superlattice and quasicrystalline ladders that possess nonuniform bond lengths, in order to study the formation of localized currents. By using density matrix renormalization group (DMRG) to characterize the quantum phases, we confirm the presence of the usual vortex and Meissner distributions of current, in which particles circulate within the bulk and around the edge respectively. Furthermore, it is also possible to observe variations to these patterns; which combine both vortex and Meissner order, and the onset of incompressible domains for specific fillings of the lattice. If the bond lengths of a ladder fluctuate, we find substantial differences to the structure of currents. This is a consequence of an inhomogeneous, effective magnetic flux, resulting in preferential localization of currents throughout the lattice bulk, towards the smaller bond lengths. We then find that incompressible domains can significantly grow in size extent across the parameter space, with currents no longer possessing an extended structure across the longitudinal direction of the ladder.

DOI: [10.1103/PhysRevResearch.5.023195](https://doi.org/10.1103/PhysRevResearch.5.023195)

I. INTRODUCTION

The Hofstadter model is a well-studied problem that describes the motion of charged particles on a 2D lattice when an external, homogeneous magnetic field is present. This model was first studied by Harper and Hofstadter [1,2], and has a fractal structure to the energy spectrum versus magnetic flux, in the form of a Hofstadter butterfly. The single-particle properties have been relatively well studied for a variety of lattice geometries, including the presence of flat bands [3,4], spectral evolution [5–8], and the appearance of topological edge states [9–11]. The extension of the Hofstadter model to include interactions between particles is an interesting problem to consider, as it can allow for the formation of quantum phases with exotic distributions of current, i.e., phases with a preferential flow of tunneling. For bosons, this was first studied in the context of Josephson junction arrays [12–16]. More recently, there has been interest in the use of ultracold gases to emulate these properties. By trapping bosonic atoms in an optical lattice, it has been possible to realize highly controllable experimental frameworks that simulate Bose-Hubbard models [17,18]. However, due to atoms being charge neu-

tral, magnetic fields must be introduced by artificial means. This has included the use of rotating Bose-Einstein condensates [19–22] and geometrically squeezed extensions [23,24], laser assisted processes [25–28], driven systems [29–32], and internal degrees of freedom [33–36]. By employing these techniques, it has been possible to realize interacting Hofstadter models with bosons [37–40], usually for square or periodic geometries. On the other hand, recent studies have shown that Fermi-Hubbard models can be simulated with optical lattices [41–43]. Fermionic systems are also predicted to host unique properties and phases when a magnetic field is present [44–47], and this has been the focus of several experimental works with ultracold fermions [48–51].

The consideration of ladder geometries represents a toy model to probe the interplay between interactions and an applied magnetic field. Indeed, the first experimental observation in ultracold atoms of chiral currents was reported by Atala *et al.* in 2014 [52] for a ladder. Further works since then have studied the numerical and theoretical properties in detail using DMRG [53–59] and bosonization techniques [60–64], with particular interest in the underlying distributions of current for different quantum phases. In relation to the currents, topological invariants have also been measured in ladder systems, notably the many-body Chern number [65–68]. For the aforementioned studies, the geometry of the ladder itself is assumed to be uniform, with no underlying spatial dependence of the model parameters. For this paper, we will consider a range of ladder geometries, which are not uniform, including those that are quasiperiodic. By varying the horizontal bond lengths of a ladder, it is possible to introduce another

*dean.johnstone@polytechnique.edu

Published by the American Physical Society under the terms of the [Creative Commons Attribution 4.0 International](https://creativecommons.org/licenses/by/4.0/) license. Further distribution of this work must maintain attribution to the author(s) and the published article's title, journal citation, and DOI.

form of preferential localization into the system. In particular, within a single-particle picture, it is known that nonuniform, quasiperiodic lattices can host in-gap, topological states that are localized in the bulk, rather than the edge. [69,70]. It is natural to expect other exotic properties to arise on nonuniform ladders when interactions are present.

Here, we present our results as follows. In Sec. II, we introduce the different kinds of Hofstadter ladder geometries for interacting bosons and discuss how ground states can be found via DMRG. Following on from this, we then outline several order parameters that can be used to characterize different quantum phases and current distributions in Sec. III. We then show our first set of results in Sec. IV, which focuses on the behavior and locality of currents for the ladder systems. Finally, phase diagrams are presented in Sec. V over a larger range of parameters, before we end with our conclusions in Sec. VI.

II. LADDER SYSTEMS

A. Interacting Hofstadter model

For a lattice of size $L = L_x \times L_y$ in the presence of a magnetic field, the system will be described by an interacting Hofstadter model of the form

$$\hat{\mathcal{H}} = - \sum_{\langle i,j \rangle} J_{ij} e^{i\theta_{ij}} \hat{b}_i^\dagger \hat{b}_j - \mu \sum_i \hat{n}_i + \frac{U}{2} \sum_i \hat{n}_i (\hat{n}_i - 1), \quad (1)$$

where U is the on-site energy, J_{ij} are the tunneling coefficients, μ is the chemical potential, \hat{b}_i (\hat{b}_i^\dagger) are the bosonic atom destruction (creation) operators at site i , $\langle i, j \rangle$ denotes nearest-neighbor summations across lattice bonds, and θ_{ij} are the Peierls phase factors [71]. The Peierls phases depend on the magnetic vector potential $\mathbf{A}(\mathbf{r})$, with \mathbf{r} being a spatial coordinate. Their form can be written as

$$\theta_{ij} = \int_{\mathbf{r}_j}^{\mathbf{r}_i} \mathbf{A}(\mathbf{r}) \cdot d\mathbf{r}, \quad (2)$$

where \mathbf{r}_i are coordinates of a lattice site i . By working in a Landau gauge of

$$\mathbf{A}(\mathbf{r}) = (0, Bx, 0), \quad (3)$$

with B denoting the magnetic field strength and x being the x coordinate, the Peierls phases can be expressed as

$$\theta_{ij} = \frac{\phi}{2A} (x_i + x_j)(y_j - y_i), \quad (4)$$

where (x_i, y_i) are the x/y spatial coordinates at site i and we have introduced the magnetic flux $\phi = BA$, for a reference area A that corresponds to a square tile of the lattice, see Fig. 1(a). Throughout this paper, we set $\hbar = q = 1$ and assume that the magnetic flux is measured in units of the flux quantum $\phi_0 = 2\pi$.

We will consider ladder geometries with $L_y = 2$, as depicted in Fig. 1, with two distinct horizontal bond lengths a and b . If a particle tunnels across the edges of a single tile, it will acquire an encircling phase $\Theta = \theta_{1,2} + \theta_{2,3} - \theta_{3,4} - \theta_{4,1}$, labeled according to the vertices in Fig. 1(a). Due to the geometrical dependence of the Peierls phases θ_{ij} , different horizontal bond lengths will produce distinct encircling

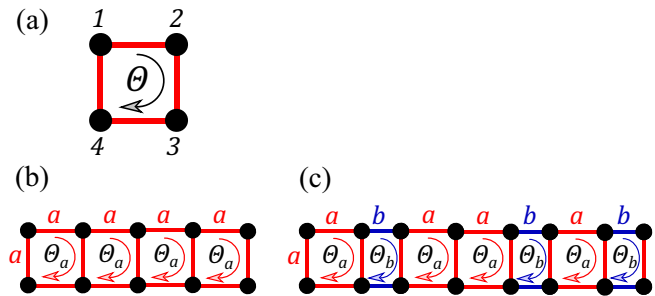


FIG. 1. Illustration of the encircling phases for different kinds of ladder systems, with bond lengths a (red) and b (blue). If a particle circulates the square tile in (a), it will acquire a unique phase factor Θ . We consider (b) uniform and (c) nonuniform distributions of a and b , which will produce the encircling phases Θ_a and Θ_b on the ladder due to the geometrical dependence of the Peierls phases in Eq. (4).

phases. Nonuniform ladders have been studied for the case of sign-staggered distributions of Θ . The staggered arrangement of Θ can be realized with ultracold atom experiments that use time-dependent fluctuations of an external potential [72]. The effective magnetic field is then zero, and chiral phases have been reported [61,72–75], in which the loop currents possess interesting, staggered structures that break time-reversal symmetry.

We will consider different distributions of the bond lengths a and b , in accordance to a binary function $X(m)$ for the m th bond. This binary sequence allows for a mapping to the horizontal bond lengths as $0 \rightarrow a$ and $1 \rightarrow b$, with an example lattice in Fig. 1(c). We will consider two distributions of $X(m)$. The first is that of a superlattice, which has the two bond lengths oscillating in a periodic manner

$$\begin{aligned} X_s(m) &= m - 1 - 2 \left\lfloor \frac{m-1}{2} \right\rfloor \\ &= [0, 1, 0, 1, 0, 1, 0, 1, \dots], \end{aligned} \quad (5)$$

where $\lfloor \dots \rfloor$ is the floor operation. We also consider a quasiperiodic distribution of bond lengths, defined by the Fibonacci word

$$\begin{aligned} X_q(m) &= 2 + \lfloor m\tau \rfloor - \lfloor (m+1)\tau \rfloor \\ &= [0, 1, 0, 0, 1, 0, 1, 0, 0, 1, \dots], \end{aligned} \quad (6)$$

where $\tau = \frac{1+\sqrt{5}}{2}$ is the golden ratio. The quasiperiodic ladder will break translational invariance, but will retain long-range order, analogous to 2D quasicrystalline tilings [76–79].

We will also incorporate a qualitative, geometrical scaling of the tunneling coefficients J_{ij} as

$$J_{ij} = \frac{J}{|\mathbf{r}_i - \mathbf{r}_j|}. \quad (7)$$

This emulates the spatial dependence of tunneling coefficients in optical lattice experiments, where it is usual for J_{ij} to scale with the relative separation between sites [80]. Note, however, that similar results can be observed without including a scaling of J_{ij} . Throughout our paper, we use the convention that sites connected by a bonds have a tunneling rate of J . In addition, vertical bonds will also have a tunneling rate of J .

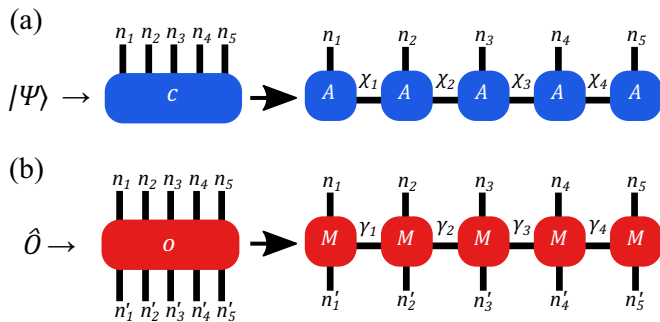


FIG. 2. Depiction of (a) a MPS and (b) MPO tensor network for a $L = 5$ 1D lattice. For each case, the many-body wavefunction $|\Psi\rangle$ and operator \hat{O} are expressed in a graphical form, with legs representing different indices of the tensors c and o . In the tensor network, c and o are rewritten as a contraction of individual tensors A or M at a lattice site, where vertical legs n_i and n'_i denote the physical dimensions at a certain site, i.e., the local Hilbert space. Finally, horizontal legs χ_i and γ_i are the bond dimensions, which capture the entanglement and correlations across the tensor network.

B. Density matrix renormalization group

Ground states of interacting models in the presence of magnetic fields can possess exotic structures and localization across the lattice. To probe these properties, we will calculate ground states numerically using the well-known framework of DMRG, which can overcome the exponential scaling of the Hilbert space in certain scenarios [81,82]. Specifically, we will adapt the matrix product state (MPS) based ansatz for the many-body wavefunction $|\Psi\rangle$, which allows for a wavefunction coefficient to be expressed as a series of contracted tensors [83,84], as per Fig. 2(a). Likewise, Hamiltonians or generic operators \hat{O} can also be expressed in a similar form, known as matrix product operators (MPOs) [85,86], shown in Fig. 2(b). In both cases, the vertical bonds of the local MPS/MPO tensors represent the local Hilbert space of a site in the Fock number basis. The horizontal bonds are known as the bond dimensions, and are used as a variational parameter to control the degree of correlations/entanglement retained within the calculation. In practice, the bond dimensions can be significantly compressed and still represent near-exact ground states [87,88] or operators [89]. In this paper, we will denote the maximum bond dimension of the MPS as D_{\max} .

To solve for the ground state, we are then interested in minimizing the Schrödinger equation

$$\langle \Psi | \hat{H} | \Psi \rangle = E \langle \Psi | \Psi \rangle, \tag{8}$$

which is depicted in Fig. 3(a) as a tensor network, where E is the eigenenergy. For practical purposes, a single tensor is usually removed from one of the MPS networks in Fig. 3(b), allowing for the minimization procedure to be reduced to an eigenvalue problem for a local site, as per Fig. 3(c). Given an initial wavefunction, the ground state can then be found by optimizing each local MPS tensor for each site until the energy converges. This is done by performing a series of left-to-right and right-to-left sweeps across the MPS tensor in Fig. 2(a). We find that 10–25 sweeps are sufficient to ensure that the energy has converged to an accuracy of 10^{-10} . Throughout this paper, we will use a maximum bond dimension D_{\max} between

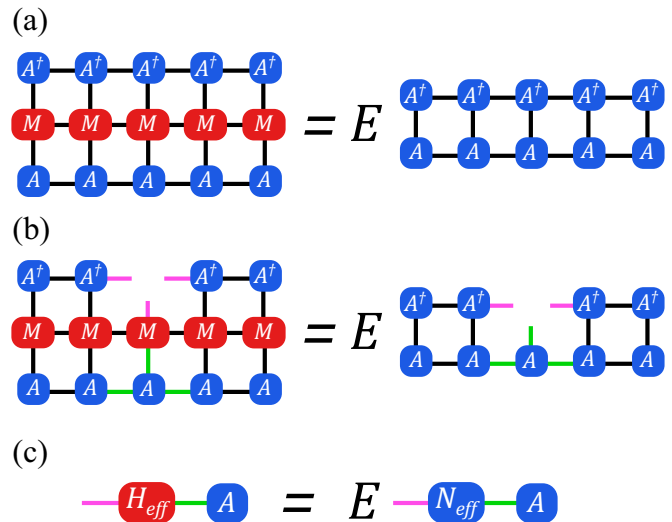


FIG. 3. Solving for the ground state, given a MPS wavefunction. We first write Eq. (8) as a tensor network in (a), and remove a single A^\dagger tensor from the system, which is shown in (b) for site 3. By then contracting tensors (black bonds) and fusing together the purple and green bonds, the problem can be reduced to a generalized eigenvalue problem $H_{\text{eff}}A = EN_{\text{eff}}A$. In practice, gauge transforms of the MPS can also transform $N_{\text{eff}} \rightarrow I$, where I is the identity matrix, which instead produces a standard eigenvalue problem.

10–300, depending on the range of parameters and resolution of phase diagrams. We also truncate singular values of the MPS that are below a threshold of 10^{-9} . Since we work in the grand canonical ensemble, D_{\max} must not be exceedingly large for practical calculations. However, as we will show in the next section and the results, our observables will be most sensitive to short-range correlations, which converge faster for smaller D_{\max} .

Typically, DMRG algorithms are applied to 1D lattice models. However, their extension to higher dimensions is also possible, provided an effective 1D mapping does not generate long-range terms between highly correlated tensors. We illustrate this idea in Fig. 4 for a ladder system. In 1D, the ladder system then has nearest-neighbor tunneling for processes in the y direction and next-nearest-neighbor tunneling for processes in the x direction.

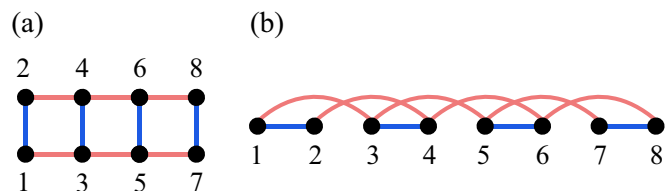


FIG. 4. 1D mapping of lattice sites and bonds for a $L = 2 \times 4$ square lattice. Each site has a unique index between 1 and L , which are mapped to the effective 1D system in (b). Red and blue connections between sites denote the horizontal (x direction) and vertical (y direction) bonds respectively.

III. OBSERVABLES AND PHASES

Given a MPS ground state, it is possible to probe a range of observables that can characterize the structure and localization of quantum phases. First, the correlation function of a state can be calculated as

$$c_{ij} = \langle \hat{b}_i^\dagger \hat{b}_j \rangle, \quad (9)$$

which can reveal the presence of quantum correlations. In experiments, the correlation function is closely linked to the Fourier transformed density profile, which has the form

$$n(\mathbf{k}) = \frac{1}{L} \sum_{ij} e^{i\mathbf{k} \cdot (\mathbf{r}_i - \mathbf{r}_j)} \langle \hat{b}_i^\dagger \hat{b}_j \rangle, \quad (10)$$

where \mathbf{k} is a wavevector. The density profile $n(\mathbf{k})$ is especially relevant for experimental protocols with ultracold atoms, as it can be directly measured from time-of-flight absorption images [18,90,91]. Note, since we consider a ladder system, we do not have a continuous set of momenta across the y direction, hence \mathbf{k} does not correspond to the momentum distribution of the ground state. Instead, \mathbf{k} represents the laser wavevector associated to a time-of-flight image with periodically repeating and decoupled ladders across y . These procedures can be used to identify whether or not a given phase is a Mott insulator (MI) or superfluid (SF) [17,18]. A SF possesses long-range correlations, resulting in a $n(\mathbf{k})$ with a sharp peak at $|\mathbf{k}| = 0$. The compressibility

$$\kappa = \frac{1}{L} \frac{\partial \langle \hat{N} \rangle}{\partial \mu} \quad (11)$$

will be finite, with $\langle \hat{N} \rangle$ the total particle number. The MI contains no correlations, and instead has a flat $n(\mathbf{k})$ due to particle immobility. As a result, κ is zero and the phase will be incompressible. The interacting Hofstadter model is known to host different kinds of incompressible phases from the usual MI. This can include charge density waves [57,92,93], incompressible Meissner or vortex domains [53,60], and topologically nontrivial Chern insulators or quantum Hall states [61,93–96]. While these phases are incompressible, they will typically contain finite currents and noninteger on-site densities. Due to this support of inherent transport, we will generally refer to these phases as incompressible, rather than insulating, i.e., the transport/currents are robust against particle number fluctuations.

A. Current distributions

Charged particles in a magnetic field will flow in a cyclical manner, meaning that there is a preferential flow of tunneling, or current present in the system. This can be quantified from Heisenberg equation of motion for the on-site densities

$$\frac{d\hat{n}_i}{dt} = i[\hat{\mathcal{H}}, \hat{n}_i] \equiv \sum_j \hat{j}_{ij}, \quad (12)$$

where the sites (i, j) are connected by bonds and the current operator \hat{j}_{ij} between sites is defined as

$$\hat{j}_{ij} = iJ_{ij}e^{i\theta_{ij}}\hat{b}_i^\dagger\hat{b}_j - \text{H.c.} \quad (13)$$

The expectation values of \hat{j}_{ij} denote local bond currents in the system, and will be the key order parameters in classifying different patterns of current that appear within MI or SF phases. From these, we can first define an average absolute current across vertical bonds as

$$|j_V| = \frac{1}{L_x} \sum_{x_i=x_j=0} |j_{ij}|, \quad (14)$$

where $j_{ij} = \frac{\langle \hat{j}_{ij} \rangle}{J_{ij}}$ and the summation only accounts for lattice sites connected across the y direction, i.e., if the $x_i = x_j$. In a similar manner, average row currents (denoted by the subscript r or R) across the x direction can be defined as

$$j_r^m = \frac{1}{L_x - 1} \sum_{x_i=(m-1)L_y, y_i=y_j=0} j_{ij} \quad (15)$$

and

$$|j_R^m| = \frac{1}{L_x - 1} \sum_{x_i=(m-1)L_y, y_i=y_j=0} |j_{ij}|, \quad (16)$$

where j_r^m is the average current across row m that takes into account the sign of each j_{ij} , and j_R^m is the average absolute current across row m that takes the absolute value of each j_{ij} . The summations for j_r^m and j_R^m only account for sites with the same y coordinate, for fixed $x_i = (m-1)L_y$, i.e., a row of the ladder. From this, the average absolute current across all horizontal bonds can then be written as

$$|j_H| = \frac{1}{L_y} \sum_m^{L_y} |j_R^m|. \quad (17)$$

Furthermore, we can also characterize a Meissner, or chiral current in the system as

$$j_M = \frac{1}{2L_y} (j_r^1 - j_r^2), \quad (18)$$

which determines the current encircling the two horizontal rows of the ladder. Note that the extra prefactor of 2 in the denominator is introduced to ensure that $|j_M| \leq |j_H|$, which will be important for the discussion of current distributions later in this section.

To better characterize the localization of bond currents across the ladder, we will also look at current locality functions. The first measure we use determines the proportion of localized currents within the ladder j_L , i.e.,

$$j_L = \frac{1}{L} \sum_{i=1}^L S_i. \quad (19)$$

Here, S_i is a discrete function for each site. If all of the bond currents j_{ij} connected to a site i are nonzero, S_i is assigned a value of 0. Otherwise, we assign a value of 1 to S_i when there is one $j_{ij} = 0$ from site i . From this function, $j_L = 0$ corresponds to all bonds of the ladder possessing finite currents j_{ij} . Similarly, $j_L = 1$ means that all sites have at least one bond with $j_{ij} = 0$. If $0 < j_L < 1$, we then have a measure that determines the fraction of blocked current channels across the ladder, i.e., the localization of currents.

Next, we also calculate the locality of finite currents across the vertical rungs of the ladder. This measure, denoted as j_E is

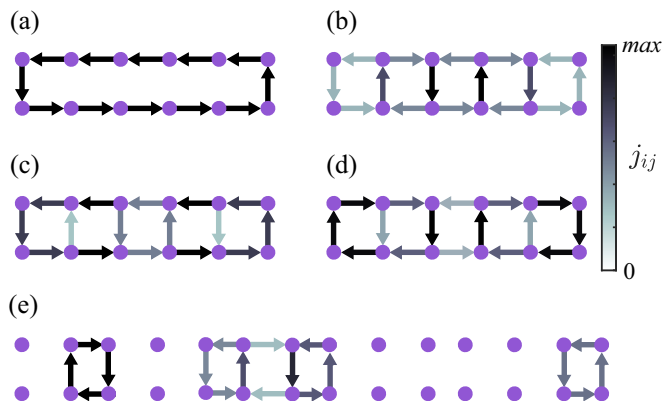


FIG. 5. Examples of currents patterns on a [(a)–(d)] $L = 2 \times 6$ periodic ladder and (e) $L = 2 \times 14$ quasiperiodic ladder, where purple circles indicate lattice sites. Currents are normalized between 0 and the maximum value, with arrows denoting paths of positive current between bonds. We show (a) Meissner pattern when $J/U = 0.4$, $\mu/U = 0.5$, $\phi/\phi_0 = 1/4$, (b) vortex pattern when $J/U = 0.44$, $\mu/U = 0.2$, $\phi/\phi_0 = 1/2$, (c) strong vortex-Meissner pattern when $J/U = 0.4$, $\mu/U = 0.8$, $\phi/\phi_0 = 1/4$, (d) weak vortex-Meissner pattern when $J/U = 0.4$, $\mu/U = 0.6$, $\phi/\phi_0 = 1/3$, and (e) localized pattern when $J/U = 0.29$, $\mu/U = 0.86$, $\phi/\phi_0 = 1/2$.

calculated by taking the average position of vertical currents, where the coordinates are normalized between 0 (centre of ladder) and 1 (edges of ladder). If a phase has finite currents across all bonds, $j_L = 0$ and

$$j_E = \frac{2}{L_x \lfloor L_x/2 \rfloor} \sum_{n=0}^{\lfloor L_x/2 \rfloor} n \approx 0.5. \quad (20)$$

On the other hand, if currents are absent across certain bonds, both j_E and j_L can take unique values. For currents with edge localization across the x direction, both j_E and j_L will converge to 1. For other kinds of localized currents, $j_E \neq 1$ and $j_L > 0$. To better illustrate these ideas, we will now turn our attention to the current distributions that may arise in the interacting Hofstadter model.

Interacting lattice models in the presence of magnetic fields will give rise to exotic distributions of current, in conjunction with the usual MI and SF phases of Bose-Hubbard models. The two primary current distributions are that of the bosonic Meissner and vortex arrangements [16], which are based on the Meissner effect [97,98] and Abrikosov vortices [99–101] for type-I and type-II superconductors. In a Meissner domain, currents are localized towards the edges of a ladder, as shown in Fig. 5(a). Currents across vertical bonds will effectively be zero, apart from the left/right edges, i.e., $|j_V| \approx 0$ and both j_E and j_L are ≈ 1 . Furthermore, currents across horizontal bonds lie in equal but opposite directions for each row of the ladder, which produces a finite Meissner current $|j_M|$.

The vortex pattern will have a similar structure to the one in Fig. 5(b). Here, all horizontal currents will be antialigned, leading to a zero Meissner current. Vertical currents are also finite, leading to a finite value of $|j_V|$. For certain parameter regimes of μ/U and ϕ/ϕ_0 , we also find several variations of the vortex pattern that incorporates a degree of Meissner ordering, with examples in Figs. 5(c) and 5(d). These are

TABLE I. Different distributions of current that can arise in the interacting Hofstadter model. For the trivial pattern, j_E is undefined (*und.*) due to the absence of currents.

Type	$ j_M $	$ j_V $	$ j_H $	j_E	j_L
Vortex (V)	= 0	> 0	> 0	= 0.5	= 0
Meissner (M)	> 0	= 0	= $ j_M $	= 1	= 1
Strong vortex-Meissner (sVM)	> 0	> 0	= $ j_M $	= 0.5	= 0
Weak vortex-Meissner (wVM)	> 0	> 0	< $ j_M $	= 0.5	= 0
Trivial (T)	= 0	= 0	= 0	<i>und.</i>	= 1

referred to as vortex-Meissner patterns with strong or weak order, depending on the relative scaling of $|j_M|$ to $|j_H|$. Note that weak or strong vortex-Meissner domains are not distinct phases, but instead measure crossover domains within a vortex-Meissner pattern. For $|j_M| = |j_H|$, all horizontal rows of current are aligned in opposite directions, and the Meissner order is strong. Otherwise, if $|j_M| \leq |j_H|$, there will be an antialignment of certain horizontal currents, i.e., a weaker Meissner order. In the limiting case of $|j_M| = 0$, we simply have a vortex pattern. Finally, if no finite currents are present in the system, we simply have a standard SF or MI phase, which is trivial from the point of view of the current. In Table I, we summarize the different distributions of current that have been outlined. For finite current patterns, it is also important to note that a sign-flipped distribution of bond currents corresponds to a degenerate ground state. While the ground state is degenerate, the order parameters that have been outlined so far are not sensitive to this sign-flipping, and the DMRG algorithm will converge towards either one of these states.

Note, nonuniform bond lengths may also allow for the formation of localized currents, with an example in Fig. 5(e). The current distributions of localized domains may be that of either vortex or vortex-Meissner patterns, with $j_L > 0$ and $j_E \neq 1$. Furthermore, if κ is finite, then the phase will resemble that of a Bose-Glass (BG). The BG is a special kind of insulating phase that can appear in Bose-Hubbard models with some kind of disorder [102,103]. In a BG, there will typically be isolated SF domains, separated by extended MI regions. The lack of percolation between the SF domains leads to an absence of macroscopic phase coherence, i.e., the phase is insulating. When the SF domains percolate, the system then enters the SF phase with macroscopic phase coherence, since atoms can flow from one end of a lattice to another. There are several ways to define this coherence, such as the percolation of SF order parameters in mean-field theory [104] or winding numbers in quantum Monte Carlo for the calculation of the SF density [105]. Alternatively, DMRG can also study phase coherence by looking at the decay of correlation functions [106], or calculating the SF density based on the proportionality with the Drude weight [107,108].

IV. BEHAVIOUR OF CURRENTS

We begin our results by considering examples of ground-state phases on ladders and their scaling over a smaller range of parameters, for hard-core bosons. We will fix $L_x \approx 40$ sites, where fluctuations around this number will be introduced to

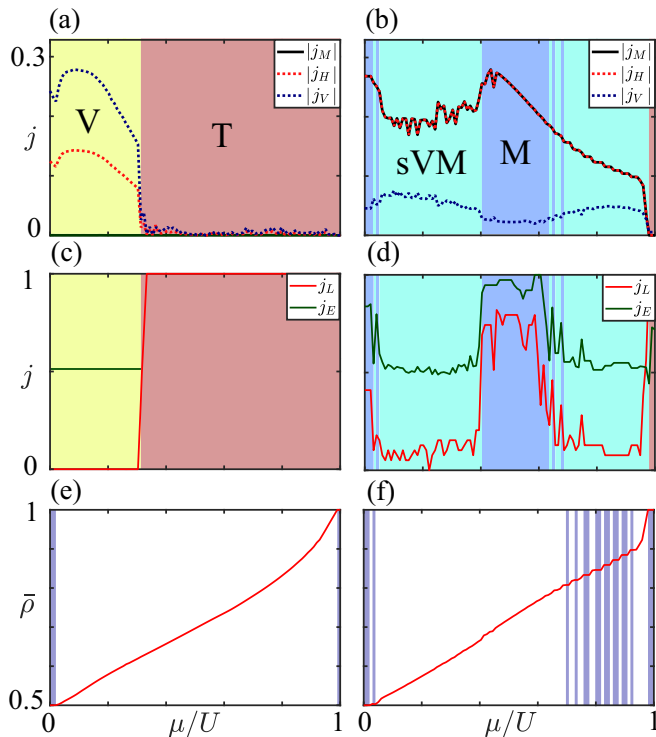


FIG. 6. Plots of [(a),(b)] current order parameters, [(c),(d)] locality measures, and [(e),(f)] the average density over a range of μ/U , with fixed [(a),(c),(e)] $J/U = 0.44$ and $\phi/\phi_0 = 0.5$, and [(b),(d),(f)] $J/U = 0.4$ and $\phi/\phi_0 = 0.25$. Current distributions are colored according to the definitions in Table I, where μ/U variations can change the underlying pattern of current. Incompressible domains are also denoted by shaded areas in (e) and (f), i.e., the plateaus of $\bar{\rho}$.

keep the system commensurate with the magnetic unit cell for superlattice and homogeneous distributions of $X(m)$. While fixed systems are considered in our main results, we note that equivalent properties have been observed for different L_x and D_{\max} , which we detail further in Appendix.

A. Homogeneous ladder ($a/b = 1$)

We will briefly cover some results for the well-studied case of homogeneous $X(m)$, where $a/b = 1$. In Fig. 6, the current order parameters are plotted for two distinct fluxes $\phi/\phi_0 = 0.5$ and $\phi/\phi_0 = 0.25$, with current patterns annotated according to Table I. For Fig. 6(a), we have $J/U = 0.44$ and $\phi/\phi_0 = 0.5$, leading to the stabilization of vortex currents for a range of μ/U , which have zero $|j_M|$. All currents will be extended across the lattice, as shown with Fig. 6(c) for $j_L = 0$ and $j_E \approx 0.5$. By increasing μ/U beyond 0.35, the currents will decay and oscillate around zero, which marks the onset of a trivial pattern. In Fig. 6(e), we also plot the average density $\bar{\rho}$, which varies continuously across a large range of μ/U , showing that the underlying phase is that of a SF. Near $\mu/U = 0$ and $\mu/U = 1$, $\bar{\rho}$ will begin to plateau, implying that $\kappa \rightarrow 0$, i.e., the onset of incompressible phases. To better understand the differences between the phases and current patterns, we also plot $n(\mathbf{k})$ in Fig. 7 at different μ/U . For Fig. 7(a) at $\mu/U = 0.98$, the $n(\mathbf{k})$ profile is relatively flat and centered at $\mathbf{k} = (0, 0)$, indicating a MI phase. When μ/U

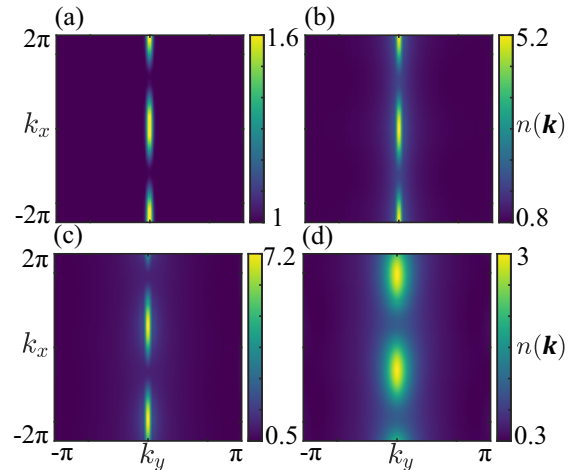


FIG. 7. $n(\mathbf{k})$ profiles, see Eq. (10), for different phases when $\phi/\phi_0 = 0.5$ and $J/U = 0.44$, including the (a) MI phase at $\mu/U = 0.98$ with trivial currents, (b) SF phase at $\mu/U = 0.6$ with trivial currents, (c) SF phase at $\mu/U = 0.15$ with vortex currents, and (d) incompressible phase at $\mu/U = 0$ with vortex currents. If the phase is incompressible, $n(\mathbf{k})$ will be relatively flat and delocalized. On the other hand, for compressible, or SF-like phases, the peak in $n(\mathbf{k})$ will become very thin and localized. When finite currents are present, the peak in $n(\mathbf{k})$ is shifted away $\mathbf{k} = (0, 0)$ due to chiral motion.

is decreased to 0.6, the system enters a SF region in Fig. 7(b), and $n(\mathbf{k})$ becomes localized to $\mathbf{k} = (0, 0)$, denoting the onset of long-range correlations. By further tuning $\mu/U = 0.15$ into the vortex region, $n(\mathbf{k})$ in Fig. 7(c) will be shifted to $\mathbf{k} \approx (\pi/2, 0)$ due to the presence of chiral currents. As we enter the other incompressible domain in Fig. 7(d) at $\mu/U = 0$, we observe similar properties, but with a shifted peak in $n(\mathbf{k})$ to $\mathbf{k} \approx (-5\pi/8, 0)$ due to a sign-flipping of currents. Finally, this $n(\mathbf{k})$ is also more extended when compared against SF phases, analogous to the MI from Fig. 7(a).

By tuning the magnetic flux, it is possible to change the distributions of current within the system, as shown in Fig. 6(b) for $\phi/\phi_0 = 0.25$ and $J/U = 0.4$. Note, this value of J/U is chosen such that when $\mu/U \approx 1$, the currents will become zero, i.e., a trivial pattern. We also plot $n(\mathbf{k})$ profiles again in Fig. 8 for this case. The Meissner current $|j_M|$ is now finite for the considered flux, with an incompressible phase for $\mu/U < 0.1$. By inspecting the locality measures in Fig. 6(d), we observe that $j_L \gg 0$ and $j_E \rightarrow 1$, implying the absence of bulk currents and formation of Meissner order. Due to this, the $n(\mathbf{k})$ profile in Fig. 8(a) possesses two distinct and symmetric peaks [109], which are extended along k_x at $k_y \approx \pm 3\pi/16$. For $0.1 \leq \mu/U \leq 0.4$, the vertical currents $|j_V|$ in the bulk will increase, marking the onset of a strong vortex-Meissner pattern, since horizontal currents are aligned on each row, i.e., $|j_M| = |j_H|$. The corresponding $n(\mathbf{k})$ in Fig. 8(b) is then more localized as a result of this. When $0.4 \leq \mu/U \leq 0.65$, the locality measures will again fluctuate near 1, revealing the formation of Meissner currents, with sharp peaks in $n(\mathbf{k})$, as per Fig. 8(c). Finally, for $\mu/U > 0.65$, we enter an interesting domain in which many distinct incompressible phases appear. By inspecting Fig. 8(f), each incompressible phase

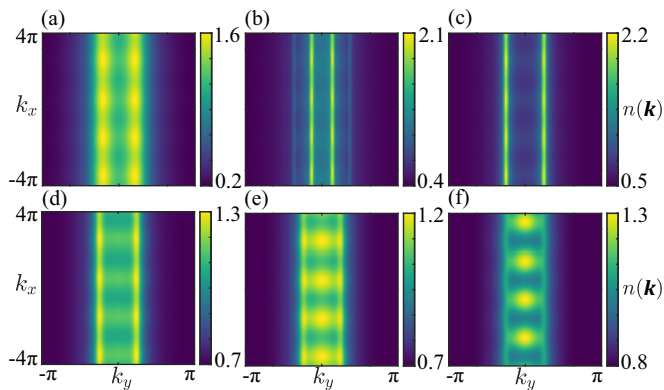


FIG. 8. $n(\mathbf{k})$ profiles, see Eq. (10), for different phases when $\phi/\phi_0 = 0.25$ and $J/U = 0.4$, including the (a) incompressible phase at $\mu/U = 0$ with Meissner currents, (b) SF phase at $\mu/U = 0.2$ with strong vortex-Meissner currents, (c) SF phase at $\mu/U = 0.5$ with Meissner currents and several incompressible phases at (d) $\mu/U = 0.77$, (e) $\mu/U = 0.84$, and (f) $\mu/U = 0.9$, which contain strong vortex-Meissner currents. SF phases with Meissner order contain two degenerate $n(\mathbf{k})$ peaks, which extend across multiple Brillouin zones. At larger μ/U , a range of incompressible phases can also form, which possess finite currents.

corresponds to the different plateaus in $\bar{\rho}$, which all have a strong vortex-Meissner current pattern. This is also reflected in the $n(\mathbf{k})$ profiles from Figs. 8(d)–8(f), which combine characteristics from both vortex and Meissner domains. For each flux, we have observed that the currents j_{ij} and density $\bar{\rho}$ vary continuously as a function of μ/U across different current domains. It should be noted, however, that the small width incompressible domains for $\mu/U > 0.65$ are almost absent for larger system sizes, which we show in Appendix A 2, Figs. 19 and 20.

B. Inhomogeneous ladders ($a/b = 2$)

Here, we will now study the influence of inhomogeneous $X(m)$ throughout the lattice, with the distributions of bond length defined from the two cases outlined in Sec. II, i.e., the superlattice and quasiperiodic ladders. We plot the behavior of currents for these ladders in Fig. 9 over a range of μ/U and J/U , for $a/b = 2$ and fixed ϕ/ϕ_0 . The superlattice distribution is first considered in Figs. 9(a) and 9(b), which shows that extended vortex-Meissner domains appear with far greater frequency. As a consequence, the Meissner distribution for the superlattice is no longer stable in these regions, being replaced by either strong or weak vortex-Meissner currents. By considering a quasiperiodic ladder in Figs. 9(c) and 9(d), similar properties are observed, with the strong vortex-Meissner pattern dominating at $\phi/\phi_0 = 0.25$. For $\phi/\phi_0 = 0.5$, however, Meissner currents are suppressed on the quasiperiodic ladder, leading to the more frequent appearance of vortex distributions. Similar to before, bond currents j_{ij} will vary continuously between different patterns of current.

To better understand the differences between homogeneous and inhomogeneous ladders, we also consider the locality

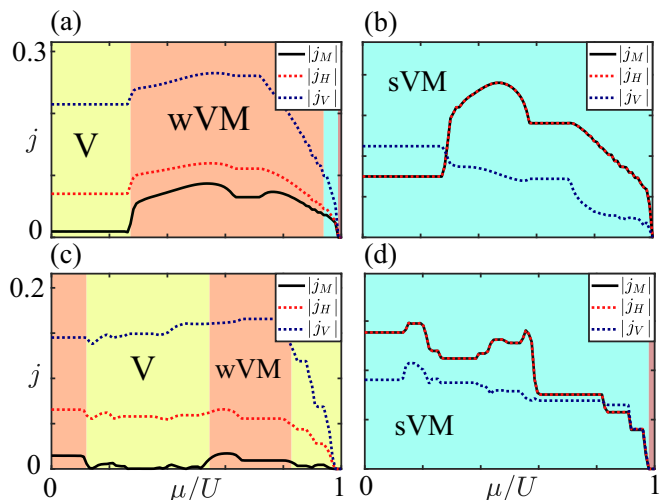


FIG. 9. Plots of current order parameters over a range of μ/U for [(a),(b)] superlattice and [(c),(d)] quasiperiodic ladders when $a/b = 2$. We consider fixed [(a),(c)] $J/U = 0.29$, $\phi/\phi_0 = 0.5$ and [(b),(d)] $J/U = 0.28$, $\phi/\phi_0 = 0.25$, with current domains colored according to the definitions in Table I. Due to the nonuniform $X(m)$, significant differences can be observed with the currents, with the vortex-Meissner patterns now dominant.

measures in Fig. 10. For the superlattice in Figs. 10(a) and 10(b), we find that most currents are extended across the lattice, with $j_E \approx 0.5$ and $j_L \approx 0$. Fluctuations will occur near $\mu/U \rightarrow 1$, which then marks the onset of more localized current distributions. On the other hand, the quasiperiodic ladder in Figs. 10(c) and 10(d) contains a higher degree of localized currents across all μ/U . This is a consequence of

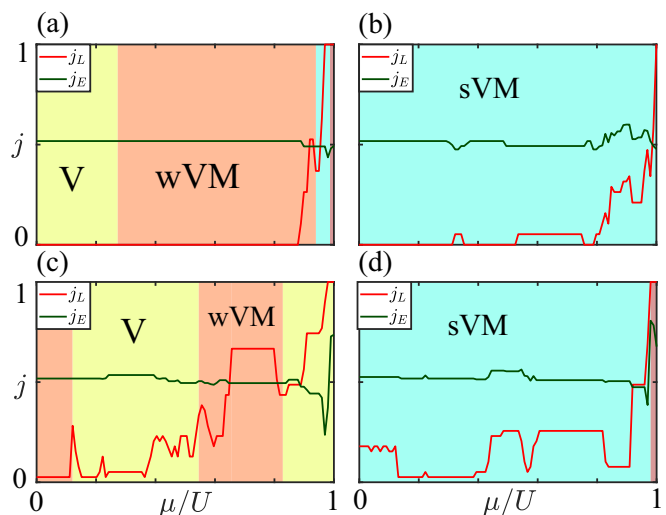


FIG. 10. Current locality measures j_L and j_E for [(a),(b)] superlattice and [(c),(d)] quasiperiodic ladders, using the same parameters and boundaries as Fig. 9. Current domains are colored according to the definitions in Table I. The superlattice ladder has the majority of phases extended across the system, indicated by $j_E \approx 0.5$ and $j_L \approx 0$. On the other hand, for the quasiperiodic ladder, fluctuations in j_L are more significant, marking the onset of localized phases.

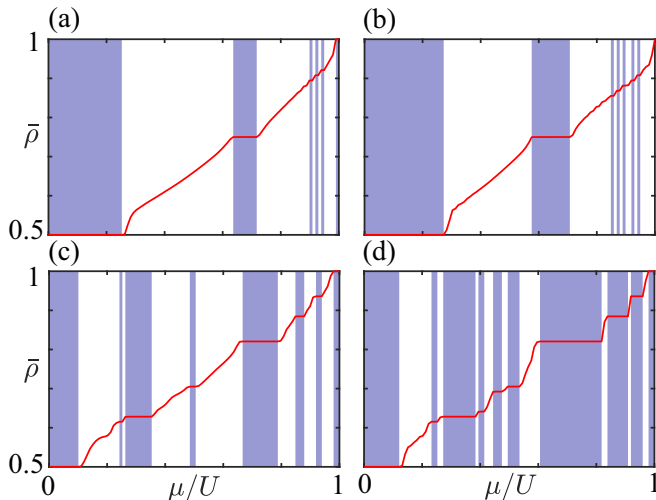


FIG. 11. Average density $\bar{\rho}$ for [(a),(b)] superlattice and [(c),(d)] quasiperiodic ladders, using the same parameters and boundaries as Fig. 9. The shaded areas highlight the incompressible phases, i.e., the plateaus in $\bar{\rho}$. In both cases, inhomogeneous ladders can stabilize extended incompressible domains. These properties are further exaggerated for the quasiperiodic ladder.

the inhomogeneous $X(m)$ distribution, which induces a form of preferential localization into the system. While the superlattice lacks this kind of localization, the inhomogeneous Peierls phases and tunneling rates can still allow for changes to the current patterns and support of vortex-Meissner domains.

Finally, we will consider the extent of incompressible phases, which can be found by plotting $\bar{\rho}$ in Fig. 11. We observe that the superlattice in Figs. 11(a) and 11(b) can contain extended, incompressible domains at far greater frequency when compared against the homogeneous system in Fig. 6. This includes an incompressible phase at half-filling for $\mu/U < 0.3$ and smaller domains for $\mu/U > 0.6$. For a quasiperiodic lattice, the incompressible phases are found to be far more dominant, as shown in in Figs. 11(c) and 11(d). For certain ϕ/ϕ_0 , it is also possible for the incompressible phases to appear more commonly than that of the SF. Furthermore, our finite-size scaling analysis in Appendix A 2, Figs. 21 and 22, reveals that the incompressible domains with widths greater than roughly $0.01\mu/U$ do not become smaller when L_x is increased. This strongly contrasts the results of the homogeneous ladder, in which incompressible phases on approach to the thermodynamic limit are only stable near $\mu/U = 0$.

To better visualize the incompressible phases for the inhomogeneous systems, we also plot several $n(\mathbf{k})$ profiles in Fig. 12. For the superlattice phases in Figs. 12(a)–12(c), two symmetric peaks will again appear around $k_x = 0$, which vary in structure and extent for different μ/U and ϕ/ϕ_0 . When $k_y \rightarrow \pm 2\pi$, we also observe the formation of separate stripe features due to the presence of inhomogeneous $X(m)$. The quasiperiodic states in Figs. 12(d)–12(f) share similar properties, although the degenerate peak across k_x tends to collapse towards $k_x = 0$. Note that while we have considered time-of-flight profiles of incompressible phases, the compressible

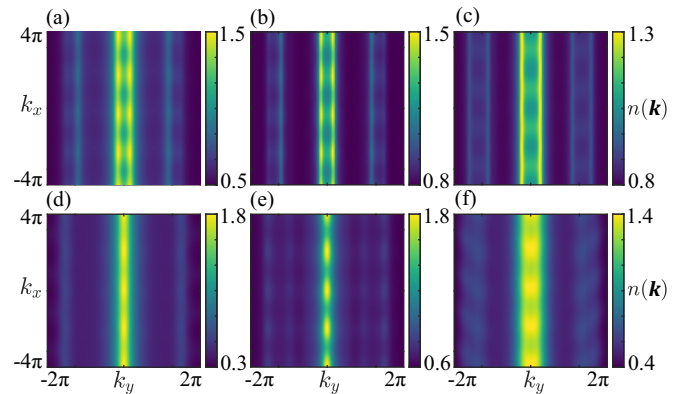


FIG. 12. $n(\mathbf{k})$ profiles, see Eq. (10), of incompressible phases for [(a)–(c)] superlattice and [(d)–(f)] quasiperiodic ladders. The magnetic flux and tunneling are fixed to (a), (b), (d), and (e) $\phi/\phi_0 = 0.5$ and $J/U = 0.29$, and (c) and (f) $\phi/\phi_0 = 0.25$ and $J/U = 0.28$, with chemical potentials of (a) $\mu/U = 0.68$, (b) $\mu/U = 0.92$, (c) $\mu/U = 0.92$, (d) $\mu/U = 0.32$, (e) $\mu/U = 0.75$, and (f) $\mu/U = 0.52$. Fluctuating bond lengths a and b produces $n(\mathbf{k})$ with mixed vortex and Meissner characteristics.

domains are very similar in structure, but with further localization of $n(\mathbf{k})$ peaks.

For crystalline ladders, there will be no specific regions for particles to preferentially localize towards one another, generally leading to extended structures of currents. Alternatively, for a quasiperiodic ladder, fluctuations in $X(m)$ allows for localization throughout the lattice, with particular arrangements of current that are not be repeated.

By looking at the time-of-flight profiles, several distinctions can also be made between different current patterns. Any phase with finite currents will be shifted away from $\mathbf{k} = (0, 0)$. For vortex currents, these shifts will only be along the k_x direction. The reason for this can be inferred from the current pattern, e.g., Fig. 5(b). Vortex patterns will usually have $2|j_H| = |j_V|$ in correspondence to Kirchhoff's law, i.e., atoms are slower across horizontal bonds, leading to a shift in the $n(\mathbf{k})$ distribution. Meissner currents, however, will contain two degenerate momenta peaks across k_y , with the shift along k_x varying. By inspecting Fig. 5(a), Meissner patterns have two vertical currents localized around the edges. This means that atoms will possess two distinct velocities across y , leading to the two well-defined peaks in $n(\mathbf{k})$. The vortex-Meissner $n(\mathbf{k})$ can contain distinct properties from both vortex and Meissner distributions of $n(\mathbf{k})$. First, the strong vortex-Meissner pattern has pronounced $n(\mathbf{k})$ peaks, like that of the Meissner distribution, but with an envelope function that corresponds to vortex currents. The weak vortex-Meissner pattern then contains less pronounced $n(\mathbf{k})$ peaks, which also have a smaller relative separation. Both the superlattice and quasiperiodic ladder can form similar kinds of phases, with separate features forming along k_y due to the nonuniform bond lengths. For the quasiperiodic ladders, the separation between $n(\mathbf{k})$ peaks usually vanishes, with larger fluctuations in the stripe-like structure. In the future, it would be interesting to compare these features with the recent observation of crystallization in Landau gauge condensates [23,24].

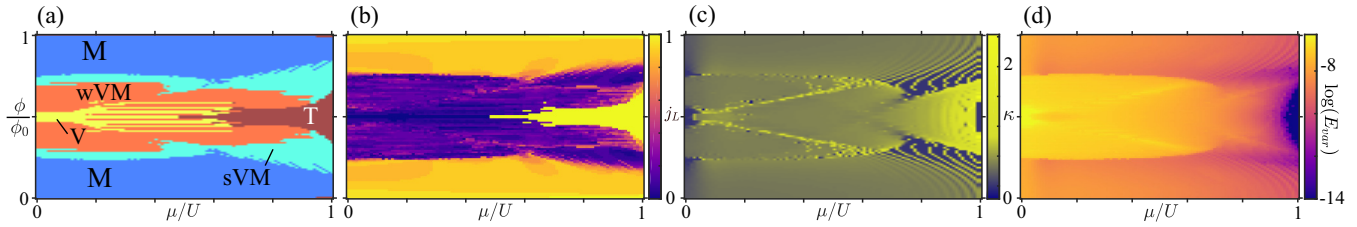


FIG. 13. Phase diagram of the homogeneous ladder for $a/b = 1$ and $J/U = 0.44$, showing the (a) current patterns, (b) locality j_L , (c) compressibility κ and, (d) energy variance E_{var} . The currents in (a) are colored for each distinct pattern in Table I. We observe a clear transition of vortex to Meissner currents, with the vortex-Meissner distributions separating their domains. For larger μ/U , sets of incompressible phases can frequently appear.

V. MAGNETIC PHASE DIAGRAMS

We will now plot full phase diagrams for the different ladders as a function of μ/U and ϕ/ϕ_0 , labeling currents according to the definitions of Table I, as before. The compressibility κ will be plotted, which can be used to visualize whether or not the system is in a SF-like or incompressible phase. This will be particularly important for the superlattice and quasiperiodic ladders, in which incompressible domains were prominent. Furthermore, inhomogeneous ladders can localize the current distributions, i.e., $j_L \gg 0$. If κ is finite when $j_L \gg 0$, we therefore have a BG-like phase, since the SF domains are separated and no longer percolate across the longitudinal direction. Finally, we will also introduce the energy variance E_{var} , which is defined by

$$E_{\text{var}} = \langle \Psi | (\hat{\mathcal{H}} - E)^2 | \Psi \rangle. \quad (21)$$

In DMRG simulations, E_{var} is a measure of how well an MPS state $|\Psi\rangle$ approximates a true eigenstate of $\hat{\mathcal{H}}$. For an exact ground state, $E_{\text{var}} = 0$. Otherwise, when D_{max} is finite, E_{var} can be a small, nonzero value, which gives a quantitative measure of how well an MPS state has converged to the true ground state.

A. Homogeneous ladder

For the first set of results, we will consider the homogeneous $a/b = 1$ ladder in Fig. 13, for fixed $J/U = 0.44$. This particular choice of J/U is chosen such that when $\mu/U \rightarrow 1$, the phase converges towards the MI phase with zero (trivial) currents. In other words, the range of μ/U we consider will characterize all finite current patterns. Phase regions over $-1 \leq \mu/U \leq 0$ will also be mirrored due to the presence of particle-hole symmetry in the hard-core, Bose-Hubbard model. In Fig. 13(a), we color different regions according to the current distributions in Table I. For $\phi/\phi_0 \approx 0.7$, there is a clear transition from the vortex to Meissner patterns of current, as has been observed in prior studies [53,55]. The current regions are also symmetric about $\phi/\phi_0 = 0.5$, in a similar manner to the single-particle Hofstadter butterfly [2]. If ϕ/ϕ_0 approaches an integer, the trivial pattern of current can be stabilized. This also occurs for a range of $\phi/\phi_0 \approx 0.5$, near $\mu/U \rightarrow 1$. Vortex-Meissner domains will also appear throughout the considered regions for smaller ranges of ϕ/ϕ_0 , and will usually separate vortex and Meissner domains. The current locality j_L is also plotted in Fig. 13(b), which further illustrates the clear transition between vortex (extended)

and Meissner (localized) currents. In other words, a $j_L \approx 1$ denotes an absence of bulk currents across vertical bonds, i.e., Meissner order. For $j_L \approx 0$, currents are fully extended, indicating variations of the vortex pattern. Fluctuations will of course arise due to the different patterns of vortex currents and changes in the magnetic unit cell. However, all phases found for the homogeneous ladder will retain an extended structure of currents throughout the lattice. Next, in Fig. 13(c), we also plot the compressibility κ , which can be used to characterize the transition between incompressible and SF phases. Here, we can see that the SF phase is usually dominant. However, we note the presence of several incompressible domains around $\mu/U = 0$, which contain vortex or Meissner current patterns. Furthermore, when $0.7 \leq \mu/U \leq 1.0$, we observe the formation of a large set of incompressible phases with vortex-Meissner patterns of current. As discussed in the previous section and Appendix A 2, the small width incompressible domains for a homogeneous ladder become vanishingly small when L_x is further increased. For all considered μ/U and ϕ/ϕ_0 , we have observed continuous behavior of the bond currents j_{ij} across different current patterns. These currents will of course be more sensitive when ϕ/ϕ_0 is changed, due to changes in the magnetic unit cell.

Finally, in Fig. 13(d), we plot the energy variance E_{var} . Generally speaking, the Meissner domains contain smaller E_{var} than that of the vortex or vortex-Meissner patterns, as indicated by the sharp change in E_{var} across $\phi/\phi_0 \approx 0.7$. This is to be expected, given the absence of bulk currents in the Meissner domains, i.e., less correlations. As we approach $\mu/U = 1$, E_{var} will also decrease, in correspondence to the onset of a trivial MI phase.

B. Superlattice ladder

Here, we now consider phase diagrams for the superlattice ladders in Fig. 14, for different values of a/b and J/U . If we first consider a small variation to $a/b = 1.25$, as per Figs. 14(a)–14(d), there are several similarities to the homogeneous ladder in terms of the general location of current distributions and incompressible domains. However, several key differences are also observed due to the inhomogeneous $X(m)$ distribution. This includes the two larger incompressible phases around $\phi/\phi_0 = 0.3$ at $\mu/U = 0.1$ and $\mu/U = 0.67$, and a restriction of the Meissner current patterns to a smaller range of ϕ/ϕ_0 below 0.2. Furthermore, the weak and strong vortex-Meissner crossover domains will then occupy larger

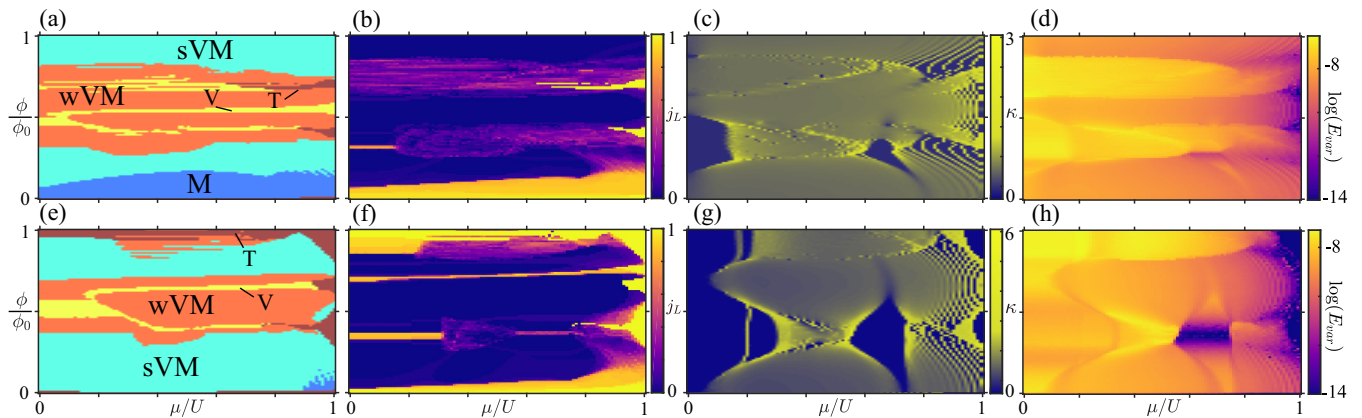


FIG. 14. Phase diagrams of the superlattice ladders for [(a)–(d)] $a/b = 1.25$ and $J/U = 0.41$, and [(e)–(h)] $a/b = 2$ and $J/U = 0.29$, showing [(a),(e)] current patterns, [(b),(f)] locality j_L , [(c),(g)] compressibility κ and, [(d),(h)] energy variance E_{var} . The currents in (a) and (e) are colored for each distinct pattern in Table I. The vortex-Meissner distributions are seen to dominate many of the phase regions when compared against the homogeneous ladder, with certain incompressible regions also growing in extent.

regions of the phase diagram, which is a consequence of inhomogeneous tunneling across the different rectangular tiles. If we inspect the current locality j_L in Figs. 14(b), it can be seen that $j_L \approx 0$ in most domains, which indicates the presence of extended currents across the lattice. When a/b is further deviated to 2 in Figs. 14(e)–14(h), these differences will be exaggerated further, with incompressible domains growing in size and overall extent. Unlike the homogeneous ladder, the incompressible domains with widths larger than $\approx 0.01\mu/U$ are stable upon further increments to L_x , as shown in Appendix 2. The Meissner distribution is also restricted to a very small range of $\phi/\phi_0 \approx 0$ in Fig. 14(e), being replaced primarily by strong vortex-Meissner domains. We also observe small values of j_L within Figs. 14(f), which again reveals the extended nature of superlattice currents.

In both cases, the variance E_{var} in Figs. 14(d) and 14(h) has similar properties to the homogeneous ladder, with smaller E_{var} towards $\mu/U = 1$ and Meissner domains. Interestingly, for $a/b = 2$, $\mu/U \approx 0.7$, and $\phi/\phi_0 \approx 0.36$, E_{var} within part of the incompressible domain is very small. By inspecting Fig. 14(f) for the same parameters, this can be linked to a higher locality of currents, or lack of correlations within the system.

C. Quasiperiodic ladder

In this final section, we will consider the phase diagrams of the quasiperiodic ladders in Fig. 15, for different values of a/b and J/U . As before, we initially consider a small variation of $a/b = 1.25$ in Figs. 15(a)–15(d), which has similar features to what was observed with the superlattice ladder in Figs. 14(a)–14(d), including the growth of incompressible phases and destabilization of the Meissner domains. However, the current locality in Fig. 14(b) tends to fluctuate around nonzero values across larger domains, showing that localized currents are forming on the quasiperiodic ladder. The differences between both homogeneous and superlattice ladders becomes significant when a larger deviation of $a/b = 2$ is used in Figs. 15(e)–15(h). For these cases, incompressible phases and strong/weak vortex-Meissner domains become far more dom-

inant across most μ/U and ϕ/ϕ_0 , as expected from Fig. 14, with the Meissner distribution being absent. Incompressible domains are also stable against finite-size fluctuations, similar to the superlattice. Furthermore, j_L in Fig. 15(f) contains a greater degree of locality away from a value of 0, which indicates the formation of intriguing, bulk localized currents. There are also several regions in which both j_L and κ are finite, which implies the formation of BG-like phases on the ladder. This is to be expected due to the absence of short-range order for the quasiperiodic ladder, i.e., different structures of current can not be repeated, and are hence localized within the bulk. We also note more prominent fluctuations in j_L across the large width incompressible domains as we vary ϕ/ϕ_0 . For these parameter regimes, the density profile does not vary. However, the underlying currents may differ in order to minimize the global energy, due to changes in the magnetic unit cell. Finally, the energy variance E_{var} in Figs. 15(d) and 15(h) shows analogous properties to that of the superlattice. In particular, for $a/b = 2$, the higher degree of current locality reduces E_{var} across larger regions of the phase diagram.

If there are multiple, distinct encircling phases Θ on a ladder, we have observed the stabilization of extended incompressible domains and localization in the system. Based on these properties, one may also infer the behavior of systems with tunneling beyond that of nearest neighbor. Such models will introduce more encircling phases Θ into the problem that now overlap one another, which will likely further stabilize incompressible domains and localization within superlattice and quasiperiodic ladders.

VI. CONCLUSIONS

In summary, we have shown that different kinds of ladder systems can possess exotic incompressible phases and localization properties. If the ladders are homogeneous or arranged as a superlattice, we observe extended and periodic structures of current across the system, with vortex and Meissner patterns dominant. On the other hand, by considering ladders with greater deviations in the bond lengths a/b , it is possible to induce dramatic shifts in the overall phase regions. For the

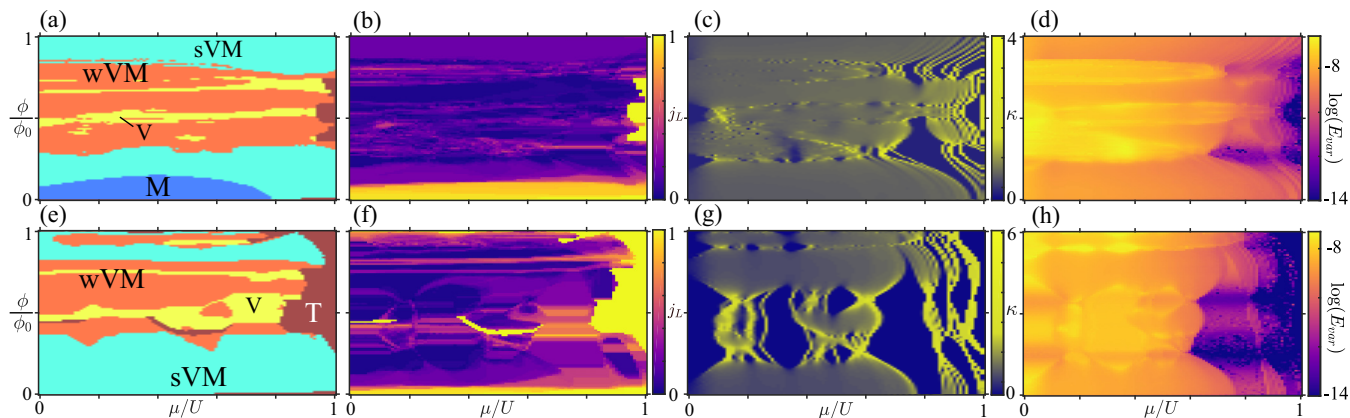


FIG. 15. Phase diagrams of the quasiperiodic ladders for [(a)–(d)] $a/b = 1.25$ and $J/U = 0.41$, and [(e)–(h)] $a/b = 2$ and $J/U = 0.29$, showing [(a),(e)] current patterns and [(b),(f)] locality j_L , [(c),(g)] compressibility κ , and [(d),(h)] energy variance E_{var} . The currents in (a) and (e) are colored for each distinct pattern in Table I. Here, the incompressible phases and vortex-Meissner domains again grow in size and extent. The locality j_L is also larger when compared to the superlattice and homogeneous ladders, which indicates the presence of localized currents.

quasiperiodic and superlattice ladders, we have seen that the weak or strong vortex-Meissner domains can become much more prominent. Furthermore, incompressible phases can occupy larger regions of the parameter space, and are robust against changes to the system size. These properties are a direct consequence of the fluctuating bond lengths and corresponding encircling phases Θ , which allows for preferential localization within the bulk, towards the smaller bond lengths. This has been made particularly clear for the case of quasiperiodic ladders, in which there is a high degree of current locality for both compressible and incompressible phases.

For future studies, we envisage that the generation of inhomogeneous fluxes could be achieved in optical lattice experiments, using similar schemes that form staggered or homogeneous fluxes [37–39,72]. As an example, it is known that time-dependent fluctuations to external potentials can artificially emulate the Peierls phases [72]. In this paper, the Peierls phases depend on the tunneling coefficients J_0 of a square optical lattice. If one instead replaces the square optical lattice with a rectangular one, the tunneling coefficients between different sites will vary, similar to Eq. (7). The reason for this is due to the dependence of J_0 on overlap integrals between Wannier functions, i.e., the radial extent of Wannier functions will fluctuate between sites.

ACKNOWLEDGMENTS

D.J. acknowledges support from EPSRC CM-CDT Grant No. EP/L015110/1. C.W.D. acknowledges support by the EPSRC Programme Grant No. DesOEQ (EP/T001062/1).

APPENDIX: CONVERGENCE OF OBSERVABLES

1. Bond dimension D_{max}

In this section, we will briefly cover some details regarding the convergence of our observables over a range of bond dimensions D_{max} . We will fix $L_x = 39$ for different ϕ/ϕ_0 , J/U , μ/U and ladder geometries. An important measure to characterize convergence of the DMRG simulations is the ground-state energy difference ΔE between different bond

dimensions, i.e., $\Delta E = (E_{D_j} - E_{D_{j+1}})/L$, where E_{D_j} is the ground-state energy when $D_{\text{max}} = D_j$, for a set of j bond dimensions. For an accurate representation of the ground state, ΔE should then be vanishingly small. To illustrate this behavior, we first consider the case of a homogeneous ladder in Fig. 16. We plot the behavior of ΔE and current order parameters at different μ/U , in order to look at the transition between different patterns of current. In particular, we have the vortex to trivial transition in Figs. 16(c) and 16(d) when $\phi/\phi_0 = 0.5$ and $J/U = 0.44$, and the strong vortex-Meissner to Meissner transition within Figs. 16(a) and 16(b) when $\phi/\phi_0 = 0.25$ and $J/U = 0.4$. Here, we can see that the relative change in energy between different bond dimensions in Figs. 16(a) and 16(c) becomes smaller as D_{max} is increased, as expected. By inspecting the current order parameters $|j_M|$,

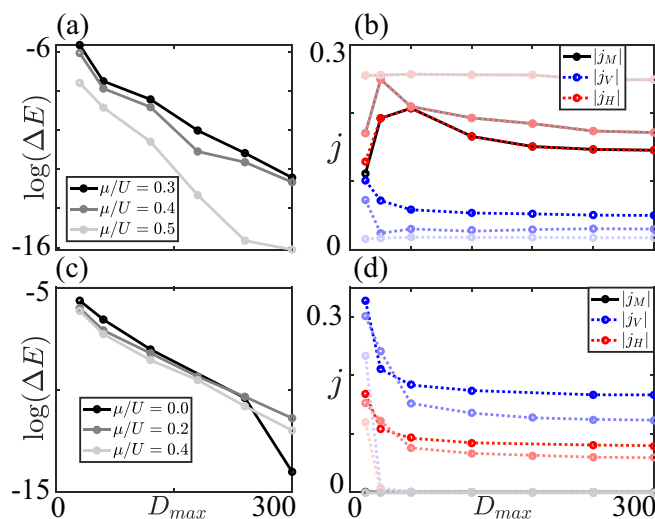


FIG. 16. Convergence of observables for the homogeneous ladder, when [(a),(b)] $\phi/\phi_0 = 0.25$ and $J/U = 0.4$ and [(c),(d)] $\phi/\phi_0 = 0.5$ and $J/U = 0.44$. Lighter shades of the curves correspond to increasing μ/U . Small variations to the observables can be seen, but the underlying current pattern does not change.

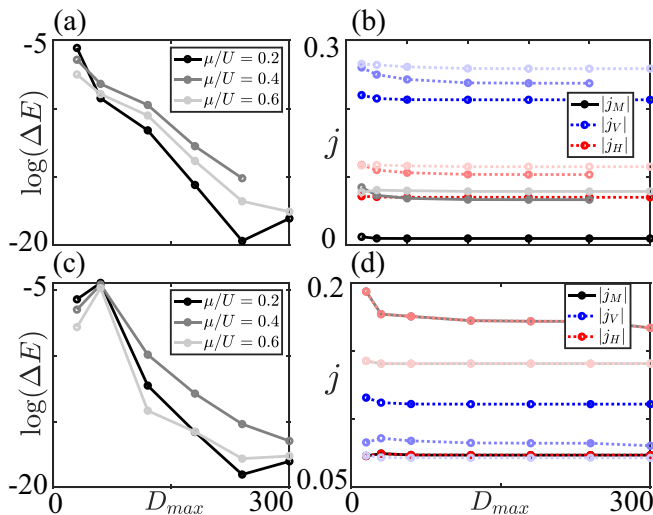


FIG. 17. Convergence of observables for the superlattice ladder with $a/b = 2$, when [(a),(b)] $\phi/\phi_0 = 0.5$ and $J/U = 0.29$ and [(c),(d)] $\phi/\phi_0 = 0.25$ and $J/U = 0.28$. Lighter shades of the curves correspond to an increasing μ/U . In all cases, we observe little variation of the order parameters between different D_{\max} .

$|j_H|$, and $|j_V|$ in Figs. 16(b) and 16(d), we can see that there are only small variations between different D_{\max} . Importantly, however, these variations do not change the underlying current patterns.

Next, we turn our attention to the inhomogeneous ladders. Similar to before, we consider the behavior of ΔE and the current observables for a superlattice ladder in Fig. 17, when $a/b = 2$. We choose a range of μ/U that encompasses different patterns of current and incompressible domains. In Figs. 17(a) and 17(b), we have $\phi/\phi_0 = 0.5$ and $J/U = 0.29$, and consider different μ/U within vortex and weak vortex-Meissner domains. Compared to the homogeneous ladder, we now observe a much faster convergence of ΔE and the current order parameters. This is likely due to the presence of nonuniform/disordered tiles within the ladder, which will reduce correlations. We also observe this faster convergence in Figs. 17(c) and 17(d) for the strong vortex-Meissner region, when $\phi/\phi_0 = 0.25$ and $J/U = 0.28$.

Finally, we plot the behavior for a quasiperiodic ladder in Fig. 18 when $a/b = 2$, for a similar range of parameters. The overall properties follow closely those that were observed within the superlattice ladder. Furthermore, for Figs. 18(c) and 18(d), we can see that the currents for $\mu/U = 0.6$ and $\mu/U = 0.8$ are equivalent, which corresponds to one of the large, incompressible domains in Fig. 11(d). In other words, the incompressible domain is stable across a range of D_{\max} .

2. System size L_x

We will now consider the influence of different L_x on the stability and extent of different current patterns and incompressible domains. As shown in the prior section, the observables and current patterns have converged over a range of bond dimensions D_{\max} . For the purposes of this section, we therefore choose a smaller $D_{\max} = 30$, and plot the

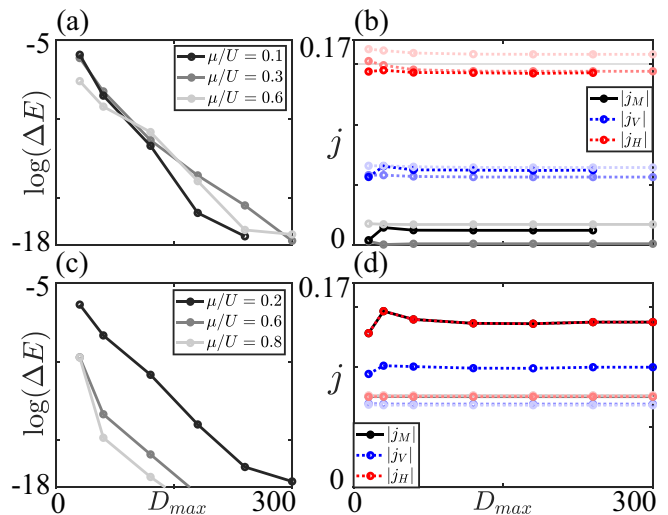


FIG. 18. Convergence of observables for the quasiperiodic ladder with $a/b = 2$, when [(a),(b)] $\phi/\phi_0 = 0.5$ and $J/U = 0.29$ and [(c),(d)] $\phi/\phi_0 = 0.25$ and $J/U = 0.28$. Lighter shades of the curves correspond to an increasing μ/U . In all cases, we observe little variation of the order parameters between different D_{\max} .

current/incompressible regions for different L_x . We start our results with the homogeneous ladder in Fig. 19, across a range of μ/U . For Figs. 19(a) and 19(c), we have strong vortex-Meissner to Meissner transitions when $\phi/\phi_0 = 0.25$ and $J/U = 0.4$. We see little variation to the current regions in

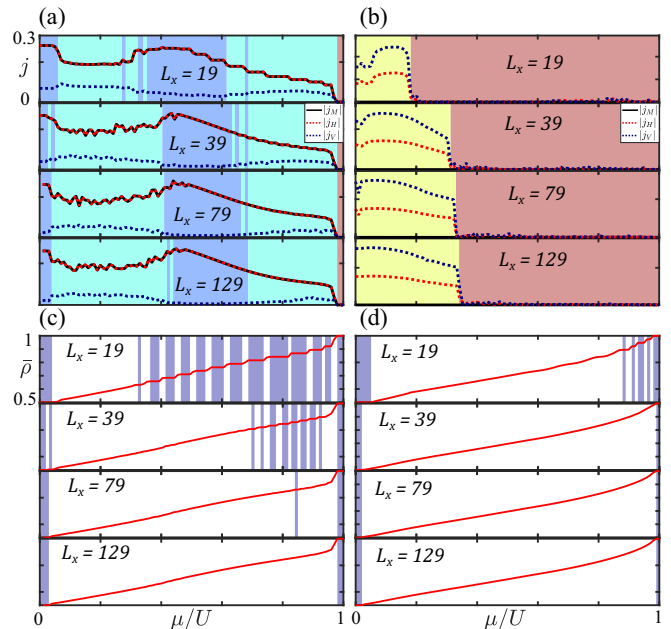


FIG. 19. Convergence of [(a),(b)] current order parameters and [(c),(d)] $\bar{\rho}$ for the homogeneous ladder with different L_x . We consider [(a),(c)] $\phi/\phi_0 = 0.25$ and $J/U = 0.4$ and [(b),(d)] $\phi/\phi_0 = 0.5$ and $J/U = 0.44$. Current patterns in (a) and (b) are colored in a similar manner to Figs. 6(b) and 6(a), with incompressible regions in (c) and (d) denoted by shaded areas. In all cases, current regions do not have strong fluctuations for increasing L_x . Incompressible windows for $\phi/\phi_0 = 0.25$ become more narrow for increasing L_x .

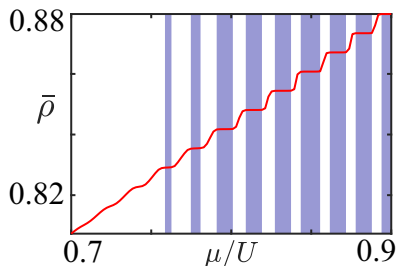


FIG. 20. Plot of the average density $\bar{\rho}$ when $L_x = 79$ for a smaller range of μ/U , but with a larger number of sampled μ/U points. Here, we can again observe the formation of incompressible domains, but they will have a much narrower extent across μ/U compared to smaller L_x .

Fig. 19(a) between different L_x . However, the incompressible domains seen in Fig. 19(c) appear to become absent when L_x is increased. It is important to note that these plots are sampled over a finite number of μ/U points, i.e., the grid of μ/U may not sample very small incompressible domains.

In Fig. 20, we plot the average density $\bar{\rho}$ when $L_x = 79$ again, but over a smaller range of μ/U , with a larger number of sampled points. Here, we see the formation of incompressible domains with very small widths, implying that the incompressible regions of the homogeneous ladder are very sensitive to particle number fluctuations. Finally, in Figs. 19(b) and 19(d), we have the vortex to trivial transi-

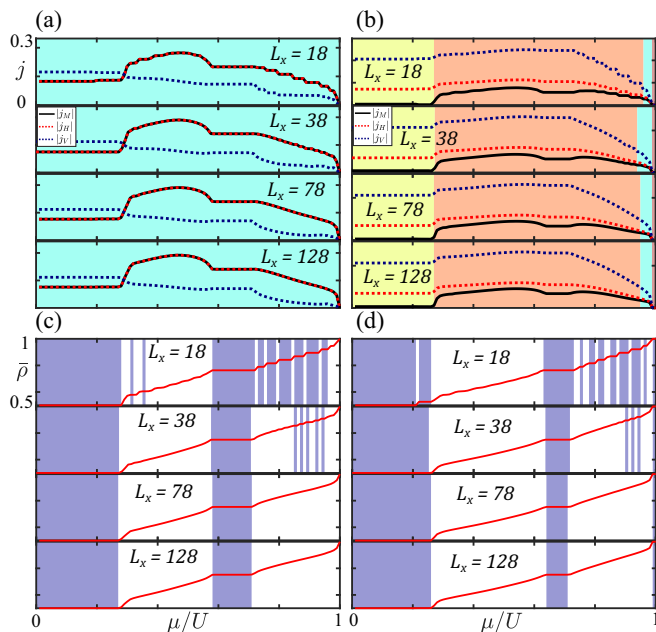


FIG. 21. Convergence of [(a),(b)] current order parameters and [(c),(d)] $\bar{\rho}$ for the superlattice ladder with $a/b = 2$ for different L_x . We consider [(a),(c)] $\phi/\phi_0 = 0.5$ and $J/U = 0.29$ and [(b),(d)] $\phi/\phi_0 = 0.25$ and $J/U = 0.28$. Current patterns in (a) and (b) are colored in a similar manner to Figs. 9(b) and 9(a), with incompressible regions in (c) and (d) denoted by shaded areas. In all cases, current regions do not have strong fluctuations for increasing L_x . Two of the larger incompressible windows do not narrow with fluctuations to L_x .

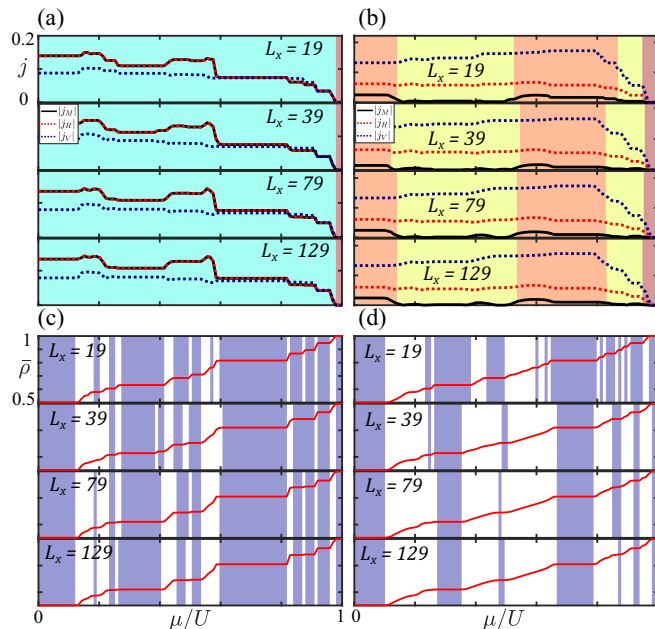


FIG. 22. Convergence of [(a),(b)] current order parameters and [(c),(d)] $\bar{\rho}$ for the quasiperiodic ladder with $a/b = 2$ for different L_x . We consider [(a),(c)] $\phi/\phi_0 = 0.5$ and $J/U = 0.29$ and [(b),(d)] $\phi/\phi_0 = 0.25$ and $J/U = 0.28$. Current patterns in (a) and (b) are colored in a similar manner to Figs. 9(d) and 9(c), with incompressible regions in (c) and (d) denoted by shaded areas. In all cases, current regions do not have strong fluctuations for increasing L_x . A larger number of incompressible domains are also retained compared to the superlattice.

tion when $\phi/\phi_0 = 0.5$ and $J/U = 0.44$, which again shows convergence of the current patterns for increasing L_x . Next, we will look at the case of superlattice ladders in Fig. 21 when $a/b = 2$. For both values of ϕ/ϕ_0 , the current order parameters and regions in Figs. 21(a) and 21(b) are stable across a range of system sizes. When considering the average density $\bar{\rho}$ in Figs. 21(c) and 21(d), we can again observe the narrowing of some incompressible domains as L_x is increased, in a similar manner to Fig. 19(c). However, compared to the homogeneous ladder, two of the larger incompressible regions around $\mu/U = 0.2$ and $\mu/U = 0.7$ do not fluctuate with changes to the system size. In Fig. 22, we perform an equivalent analysis for the case of a quasiperiodic ladder with $a/b = 2$. As expected from the discussion in our main results, the overall properties follow closely that of the superlattice ladder, with convergence of the current regions in Figs. 22(a) and 22(b) over different L_x . The average density $\bar{\rho}$ within Figs. 22(c) and 22(d) is also similar, but with the retention of a larger number of smaller, incompressible windows across μ/U . Summarizing, we have seen that our order parameters have converged over a range of system sizes L_x and bond dimensions D_{\max} , with little variation to the underlying patterns of current. For the incompressible domains, we have also observed that some of the smaller width regions in our results are sensitive to particle number fluctuations, based on the narrowing of these windows with increasing L_x . However, for the superlattice and quasiperiodic ladder we do not observe any narrowing of the largest incompressible domains.

- [1] P. G. Harper, Single band motion of conduction electrons in a uniform magnetic field, *Proc. Phys. Soc. London, Sect. A* **68**, 874 (1955).
- [2] D. R. Hofstadter, Energy levels and wave functions of Bloch electrons in rational and irrational magnetic fields, *Phys. Rev. B* **14**, 2239 (1976).
- [3] H. Aoki, M. Ando, and H. Matsumura, Hofstadter butterflies for flat bands, *Phys. Rev. B* **54**, R17296 (1996).
- [4] F. Harper, S. H. Simon, and R. Roy, Perturbative approach to flat Chern bands in the Hofstadter model, *Phys. Rev. B* **90**, 075104 (2014).
- [5] F. Yilmaz and M. O. Oktel, Hofstadter butterfly evolution in the space of two-dimensional Bravais lattices, *Phys. Rev. A* **95**, 063628 (2017).
- [6] L. Du, Q. Chen, A. D. Barr, A. R. Barr, and G. A. Fiete, Floquet Hofstadter butterfly on the kagome and triangular lattices, *Phys. Rev. B* **98**, 245145 (2018).
- [7] J. Herzog-Arbeitman, Z.-D. Song, N. Regnault, and B. A. Bernevig, Hofstadter Topology: Noncrystalline Topological Materials at High Flux, *Phys. Rev. Lett.* **125**, 236804 (2020).
- [8] J. Herzog-Arbeitman, Z.-D. Song, L. Elcoro, and B. A. Bernevig, Hofstadter topology with real space invariants and reentrant projective symmetries, *Phys. Rev. Lett.* **130**, 236601 (2023).
- [9] Y. Hatsugai, Chern Number and Edge States in the Integer Quantum Hall Effect, *Phys. Rev. Lett.* **71**, 3697 (1993).
- [10] R. Chen, C.-Z. Chen, J.-H. Gao, B. Zhou, and D.-H. Xu, Higher-Order Topological Insulators in Quasicrystals, *Phys. Rev. Lett.* **124**, 036803 (2020).
- [11] D. Varjas, A. Lau, K. Pöyhönen, A. R. Akhmerov, D. I. Pikulin, and I. C. Fulga, Topological Phases without Crystalline Counterparts, *Phys. Rev. Lett.* **123**, 196401 (2019).
- [12] E. Granato, Phase transitions in Josephson-junction ladders in a magnetic field, *Phys. Rev. B* **42**, 4797 (1990).
- [13] J. J. Mazo, F. Falo, and L. M. Floría, Josephson junction ladders: Ground state and relaxation phenomena, *Phys. Rev. B* **52**, 10433 (1995).
- [14] C. Denniston and C. Tang, Phases of Josephson Junction Ladders, *Phys. Rev. Lett.* **75**, 3930 (1995).
- [15] M. Kardar, Josephson-junction ladders and quantum fluctuations, *Phys. Rev. B* **33**, 3125 (1986).
- [16] E. Orignac and T. Giamarchi, Meissner effect in a bosonic ladder, *Phys. Rev. B* **64**, 144515 (2001).
- [17] D. Jaksch, C. Bruder, J. I. Cirac, C. W. Gardiner, and P. Zoller, Cold Bosonic Atoms in Optical Lattices, *Phys. Rev. Lett.* **81**, 3108 (1998).
- [18] M. Greiner, O. Mandel, T. Esslinger, T. W. Hänsch, and I. Bloch, Quantum phase transition from a superfluid to a Mott insulator in a gas of ultracold atoms, *Nature (London)* **415**, 39 (2002).
- [19] K. W. Madison, F. Chevy, W. Wohlleben, and J. Dalibard, Vortex Formation in a Stirred Bose-Einstein Condensate, *Phys. Rev. Lett.* **84**, 806 (2000).
- [20] J. R. Abo-Shaeer, C. Raman, J. M. Vogels, and W. Ketterle, Observation of vortex lattices in Bose-Einstein condensates, *Science* **292**, 476 (2001).
- [21] V. Schweikhard, I. Coddington, P. Engels, V. P. Mogendorff, and E. A. Cornell, Rapidly Rotating Bose-Einstein Condensates in and near the Lowest Landau Level, *Phys. Rev. Lett.* **92**, 040404 (2004).
- [22] V. Bretin, S. Stock, Y. Seurin, and J. Dalibard, Fast Rotation of a Bose-Einstein Condensate, *Phys. Rev. Lett.* **92**, 050403 (2004).
- [23] R. J. Fletcher, A. Shaffer, C. C. Wilson, P. B. Patel, Z. Yan, V. Crépel, B. Mukherjee, and M. W. Zwierlein, Geometric squeezing into the lowest Landau level, *Science* **372**, 1318 (2021).
- [24] B. Mukherjee, A. Shaffer, P. B. Patel, Z. Yan, C. C. Wilson, V. Crépel, R. J. Fletcher, and M. Zwierlein, Crystallization of bosonic quantum Hall states in a rotating quantum gas, *Nature (London)* **601**, 58 (2022).
- [25] N. Goldman, G. Juzeliūnas, P. Öhberg, and I. B. Spielman, Light-induced gauge fields for ultracold atoms, *Rep. Prog. Phys.* **77**, 126401 (2014).
- [26] G. Juzeliūnas, J. Ruseckas, P. Öhberg, and M. Fleischhauer, Light-induced effective magnetic fields for ultracold atoms in planar geometries, *Phys. Rev. A* **73**, 025602 (2006).
- [27] Y.-J. Lin, R. L. Compton, A. R. Perry, W. D. Phillips, J. V. Porto, and I. B. Spielman, Bose-Einstein Condensate in a Uniform Light-Induced Vector Potential, *Phys. Rev. Lett.* **102**, 130401 (2009).
- [28] D. Jaksch and P. Zoller, Creation of effective magnetic fields in optical lattices: The Hofstadter butterfly for cold neutral atoms, *New J. Phys.* **5**, 56 (2003).
- [29] J. Struck, C. Ölschläger, M. Weinberg, P. Hauke, J. Simonet, A. Eckardt, M. Lewenstein, K. Sengstock, and P. Windpassinger, Tunable Gauge Potential for Neutral and Spinless Particles in Driven Optical Lattices, *Phys. Rev. Lett.* **108**, 225304 (2012).
- [30] P. Hauke, O. Tieleman, A. Celi, C. Ölschläger, J. Simonet, J. Struck, M. Weinberg, P. Windpassinger, K. Sengstock, M. Lewenstein, and A. Eckardt, Non-Abelian Gauge Fields and Topological Insulators in Shaken Optical Lattices, *Phys. Rev. Lett.* **109**, 145301 (2012).
- [31] N. Goldman and J. Dalibard, Periodically Driven Quantum Systems: Effective Hamiltonians and Engineered Gauge Fields, *Phys. Rev. X* **4**, 031027 (2014).
- [32] C. E. Creffield, G. Pieplow, F. Sols, and N. Goldman, Realization of uniform synthetic magnetic fields by periodically shaking an optical square lattice, *New J. Phys.* **18**, 093013 (2016).
- [33] B. K. Stuhl, H.-I. Lu, L. M. Aycock, D. Genkina, and I. B. Spielman, Visualizing edge states with an atomic Bose gas in the quantum Hall regime, *Science* **349**, 1514 (2015).
- [34] M. Mancini, G. Pagano, G. Cappellini, L. Livi, M. Rider, J. Catani, C. Sias, P. Zoller, M. Inguscio, M. Dalmonte, and L. Fallani, Observation of chiral edge states with neutral fermions in synthetic Hall ribbons, *Science* **349**, 1510 (2015).
- [35] L. F. Livi, G. Cappellini, M. Diem, L. Franchi, C. Clivati, M. Frittelli, F. Levi, D. Calonico, J. Catani, M. Inguscio, and L. Fallani, Synthetic Dimensions and Spin-Orbit Coupling with an Optical Clock Transition, *Phys. Rev. Lett.* **117**, 220401 (2016).
- [36] H. M. Price, O. Zilberberg, T. Ozawa, I. Carusotto, and N. Goldman, Four-Dimensional Quantum Hall Effect with Ultracold Atoms, *Phys. Rev. Lett.* **115**, 195303 (2015).
- [37] M. Aidelsburger, M. Atala, S. Nascimbène, S. Trotzky, Y.-A. Chen, and I. Bloch, Experimental Realization of Strong

- Effective Magnetic Fields in an Optical Lattice, *Phys. Rev. Lett.* **107**, 255301 (2011).
- [38] K. Jiménez-García, L. J. LeBlanc, R. A. Williams, M. C. Beeler, A. R. Perry, and I. B. Spielman, Peierls Substitution in an Engineered Lattice Potential, *Phys. Rev. Lett.* **108**, 225303 (2012).
- [39] M. Aidelsburger, M. Atala, M. Lohse, J. T. Barreiro, B. Paredes, and I. Bloch, Realization of the Hofstadter Hamiltonian with Ultracold Atoms in Optical Lattices, *Phys. Rev. Lett.* **111**, 185301 (2013).
- [40] H. Miyake, G. A. Siviloglou, C. J. Kennedy, W. C. Burton, and W. Ketterle, Realizing the Harper Hamiltonian with Laser-Assisted Tunneling in Optical Lattices, *Phys. Rev. Lett.* **111**, 185302 (2013).
- [41] N. Strohmaier, Y. Takasu, K. Günter, R. Jördens, M. Köhl, H. Moritz, and T. Esslinger, Interaction-Controlled Transport of an Ultracold Fermi Gas, *Phys. Rev. Lett.* **99**, 220601 (2007).
- [42] R. Jördens, N. Strohmaier, K. Günter, H. Moritz, and T. Esslinger, A Mott insulator of fermionic atoms in an optical lattice, *Nature (London)* **455**, 204 (2008).
- [43] U. Schneider, L. Hackermüller, S. Will, T. Best, I. Bloch, T. A. Costi, R. W. Helmes, D. Rasch, and A. Rosch, Metallic and insulating phases of repulsively interacting fermions in a 3D optical lattice, *Science* **322**, 1520 (2008).
- [44] W. Zheng, Z. Zhu, D. N. Sheng, and Z.-Y. Weng, Hidden spin current in doped Mott antiferromagnets, *Phys. Rev. B* **98**, 165102 (2018).
- [45] D. Sen and R. Chitra, Large-U limit of a Hubbard model in a magnetic field: Chiral spin interactions and paramagnetism, *Phys. Rev. B* **51**, 1922 (1995).
- [46] L. Wang, H.-H. Hung, and M. Troyer, Topological phase transition in the Hofstadter-Hubbard model, *Phys. Rev. B* **90**, 205111 (2014).
- [47] P. Kumar, T. Mertz, and W. Hofstetter, Interaction-induced topological and magnetic phases in the Hofstadter-Hubbard model, *Phys. Rev. B* **94**, 115161 (2016).
- [48] H. Zhai, R. O. Umucalılar, and M. O. Oktel, Pairing and Vortex Lattices for Interacting Fermions in Optical Lattices with a Large Magnetic Field, *Phys. Rev. Lett.* **104**, 145301 (2010).
- [49] R. O. Umucalılar, H. Zhai, and M. O. Oktel, Trapped Fermi Gases in Rotating Optical Lattices: Realization and Detection of the Topological Hofstadter Insulator, *Phys. Rev. Lett.* **100**, 070402 (2008).
- [50] N. Goldman, J. Beugnon, and F. Gerbier, Detecting Chiral Edge States in the Hofstadter Optical Lattice, *Phys. Rev. Lett.* **108**, 255303 (2012).
- [51] M. Łącki, H. Pichler, A. Sterdyniak, A. Lyras, V. E. Lembessis, O. Al-Dossary, J. C. Budich, and P. Zoller, Quantum Hall physics with cold atoms in cylindrical optical lattices, *Phys. Rev. A* **93**, 013604 (2016).
- [52] M. Atala, M. Aidelsburger, M. Lohse, J. Barreiro, B. Paredes, and I. Bloch, Observation of chiral currents with ultracold atoms in bosonic ladders, *Nat. Phys.* **10**, 588 (2014).
- [53] M. Piraud, F. Heidrich-Meisner, I. P. McCulloch, S. Greschner, T. Vekua, and U. Schollwöck, Vortex and Meissner phases of strongly interacting bosons on a two-leg ladder, *Phys. Rev. B* **91**, 140406(R) (2015).
- [54] M. Di Dio, S. De Palo, E. Orignac, R. Citro, and M.-L. Chiofalo, Persisting meissner state and incommensurate phases of hard-core boson ladders in a flux, *Phys. Rev. B* **92**, 060506(R) (2015).
- [55] E. Orignac, R. Citro, M. D. Dio, S. D. Palo, and M.-L. Chiofalo, Incommensurate phases of a bosonic two-leg ladder under a flux, *New J. Phys.* **18**, 055017 (2016).
- [56] E. Orignac, R. Citro, M. Di Dio, and S. De Palo, Vortex lattice melting in a boson ladder in an artificial gauge field, *Phys. Rev. B* **96**, 014518 (2017).
- [57] S. Greschner, M. Piraud, F. Heidrich-Meisner, I. P. McCulloch, U. Schollwöck, and T. Vekua, Symmetry-broken states in a system of interacting bosons on a two-leg ladder with a uniform Abelian gauge field, *Phys. Rev. A* **94**, 063628 (2016).
- [58] S. Greschner, M. Piraud, F. Heidrich-Meisner, I. P. McCulloch, U. Schollwöck, and T. Vekua, Spontaneous Increase of Magnetic Flux and Chiral-Current Reversal in Bosonic Ladders: Swimming Against the Tide, *Phys. Rev. Lett.* **115**, 190402 (2015).
- [59] A. Haller, A. S. Matsoukas-Roubeas, Y. Pan, M. Rizzi, and M. Burrello, Exploring helical phases of matter in bosonic ladders, *Phys. Rev. Res.* **2**, 043433 (2020).
- [60] A. Petrescu and K. Le Hur, Bosonic Mott Insulator with Meissner Currents, *Phys. Rev. Lett.* **111**, 150601 (2013).
- [61] A. Petrescu and K. Le Hur, Chiral Mott insulators, Meissner effect, and Laughlin states in quantum ladders, *Phys. Rev. B* **91**, 054520 (2015).
- [62] A. Tokuno and A. Georges, Ground states of a Bose-Hubbard ladder in an artificial magnetic field: Field-theoretical approach, *New J. Phys.* **16**, 073005 (2014).
- [63] R. Wei and E. J. Mueller, Theory of bosons in two-leg ladders with large magnetic fields, *Phys. Rev. A* **89**, 063617 (2014).
- [64] S. Uchino, Analytical approach to a bosonic ladder subject to a magnetic field, *Phys. Rev. A* **93**, 053629 (2016).
- [65] M. Aidelsburger, M. Lohse, C. Schweizer, M. Atala, J. T. Barreiro, S. Nascimbène, N. Cooper, I. Bloch, and N. Goldman, Measuring the Chern number of Hofstadter bands with ultracold bosonic atoms, *Nat. Phys.* **11**, 162 (2015).
- [66] D. Genkina, L. M. Aycocock, H.-I. Lu, M. Lu, A. M. Pineiro, and I. Spielman, Imaging topology of Hofstadter ribbons, *New J. Phys.* **21**, 053021 (2019).
- [67] T. Chalopin, T. Satoor, A. Evrard, V. Makhlov, J. Dalibard, R. Lopes, and S. Nascimbene, Probing chiral edge dynamics and bulk topology of a synthetic Hall system, *Nat. Phys.* **16**, 1017 (2020).
- [68] S. Muga, A. Dauphin, P. Massignan, L. Tarruell, M. Lewenstein, C. Lobo, and A. Celi, Measuring Chern numbers in Hofstadter strips, *SciPost Phys.* **3**, 012 (2017).
- [69] D. Johnstone, M. J. Colbrook, A. E. B. Nielsen, P. Öhberg, and C. W. Duncan, Bulk localized transport states in infinite and finite quasicrystals via magnetic aperiodicity, *Phys. Rev. B* **106**, 045149 (2022).
- [70] C. W. Duncan, S. Manna, and A. E. B. Nielsen, Topological models in rotationally symmetric quasicrystals, *Phys. Rev. B* **101**, 115413 (2020).
- [71] R. Peierls, Zur theorie des diamagnetismus von leitungselektronen, *Z. Phys.* **80**, 763 (1933).
- [72] L.-K. Lim, A. Hemmerich, and C. M. Smith, Artificial staggered magnetic field for ultracold atoms in optical lattices, *Phys. Rev. A* **81**, 023404 (2010).

- [73] A. Dhar, M. Maji, T. Mishra, R. V. Pai, S. Mukerjee, and A. Paramekanti, Bose-Hubbard model in a strong effective magnetic field: Emergence of a chiral Mott insulator ground state, *Phys. Rev. A* **85**, 041602(R) (2012).
- [74] A. Dhar, T. Mishra, M. Maji, R. V. Pai, S. Mukerjee, and A. Paramekanti, Chiral Mott insulator with staggered loop currents in the fully frustrated Bose-Hubbard model, *Phys. Rev. B* **87**, 174501 (2013).
- [75] G. Möller and N. R. Cooper, Condensed ground states of frustrated Bose-Hubbard models, *Phys. Rev. A* **82**, 063625 (2010).
- [76] N. de Bruijn, Algebraic theory of Penrose's non-periodic tilings of the plane. I, *Indag. Math.* **84**, 39 (1981).
- [77] N. de Bruijn, Algebraic theory of Penrose's non-periodic tilings of the plane. II, *Indag. Math.* **84**, 53 (1981).
- [78] R. Penrose, The role of aesthetics in pure and applied mathematical research, *Bull. Inst. Math. Appl.* **10**, 266 (1974).
- [79] R. M. Robinson, Undecidability and nonperiodicity for tilings of the plane, *Invent. Math.* **12**, 177 (1971).
- [80] G. H. Wannier, The Structure of Electronic Excitation Levels in Insulating Crystals, *Phys. Rev.* **52**, 191 (1937).
- [81] S. R. White, Density Matrix Formulation for Quantum Renormalization Groups, *Phys. Rev. Lett.* **69**, 2863 (1992).
- [82] S. R. White, Density-matrix algorithms for quantum renormalization groups, *Phys. Rev. B* **48**, 10345 (1993).
- [83] S. Östlund and S. Rommer, Thermodynamic Limit of Density Matrix Renormalization, *Phys. Rev. Lett.* **75**, 3537 (1995).
- [84] J. Dukelsky, M. A. Martín-Delgado, T. Nishino, and G. Sierra, Equivalence of the variational matrix product method and the density matrix renormalization group applied to spin chains, *Europhys. Lett.* **43**, 457 (1998).
- [85] M. Zwolak and G. Vidal, Mixed-State Dynamics in One-Dimensional Quantum Lattice Systems: A Time-Dependent Superoperator Renormalization Algorithm, *Phys. Rev. Lett.* **93**, 207205 (2004).
- [86] F. Verstraete, J. J. García-Ripoll, and J. I. Cirac, Matrix Product Density Operators: Simulation of Finite-Temperature and Dissipative Systems, *Phys. Rev. Lett.* **93**, 207204 (2004).
- [87] F. Verstraete, V. Murg, and J. Cirac, Matrix product states, projected entangled pair states, and variational renormalization group methods for quantum spin systems, *Adv. Phys.* **57**, 143 (2008).
- [88] U. Schollwöck, The density-matrix renormalization group, *Rev. Mod. Phys.* **77**, 259 (2005).
- [89] C. Hubig, I. P. McCulloch, and U. Schollwöck, Generic construction of efficient matrix product operators, *Phys. Rev. B* **95**, 035129 (2017).
- [90] I. B. Spielman, W. D. Phillips, and J. V. Porto, Condensate Fraction in a 2D Bose Gas Measured Across the Mott-Insulator Transition, *Phys. Rev. Lett.* **100**, 120402 (2008).
- [91] S. Fölling, F. Gerbier, A. Widera, O. Mandel, T. Gericke, and I. Bloch, Spatial quantum noise interferometry in expanding ultracold atom clouds, *Nature (London)* **434**, 481 (2005).
- [92] S. Greschner and T. Vekua, Vortex-Hole Duality: A Unified Picture of Weak- and Strong-Coupling Regimes of Bosonic Ladders with Flux, *Phys. Rev. Lett.* **119**, 073401 (2017).
- [93] F. Grusdt and M. Höning, Realization of fractional Chern insulators in the thin-torus limit with ultracold bosons, *Phys. Rev. A* **90**, 053623 (2014).
- [94] M. Calvanese Strinati, E. Cornfeld, D. Rossini, S. Barbarino, M. Dalmonte, R. Fazio, E. Sela, and L. Mazza, Laughlin-like States in Bosonic and Fermionic Atomic Synthetic Ladders, *Phys. Rev. X* **7**, 021033 (2017).
- [95] A. Petrescu, M. Piraud, G. Roux, I. P. McCulloch, and K. Le Hur, Precursor of the Laughlin state of hard-core bosons on a two-leg ladder, *Phys. Rev. B* **96**, 014524 (2017).
- [96] A. S. Sørensen, E. Demler, and M. D. Lukin, Fractional Quantum Hall States of Atoms in Optical Lattices, *Phys. Rev. Lett.* **94**, 086803 (2005).
- [97] W. Meissner and R. Ochsenfeld, Ein neuer effekt bei eintritt der supraleitfähigkeit, *Sci. Nat.* **21**, 787 (1933).
- [98] J. Bardeen, L. N. Cooper, and J. R. Schrieffer, Theory of superconductivity, *Phys. Rev.* **108**, 1175 (1957).
- [99] J. Rjabinin and L. Shubnikow, Magnetic properties and critical currents of supra-conducting alloys, *Nature (London)* **135**, 581 (1935).
- [100] V. L. Ginzburg and L. D. Landau, On the theory of superconductivity, in *On Superconductivity and Superfluidity* (Springer, New York, 2009), pp. 113–137.
- [101] A. A. Abrikosov, Nobel lecture: Type-II superconductors and the vortex lattice, *Rev. Mod. Phys.* **76**, 975 (2004).
- [102] J. Kisker and H. Rieger, Bose-glass and Mott-insulator phase in the disordered boson Hubbard model, *Phys. Rev. B* **55**, R11981 (1997).
- [103] M. P. A. Fisher, P. B. Weichman, G. Grinstein, and D. S. Fisher, Boson localization and the superfluid-insulator transition, *Phys. Rev. B* **40**, 546 (1989).
- [104] A. Niederle and H. Rieger, Superfluid clusters, percolation and phase transitions in the disordered, two-dimensional Bose-Hubbard model, *New J. Phys.* **15**, 075029 (2013).
- [105] E. L. Pollock and D. M. Ceperley, Path-integral computation of superfluid densities, *Phys. Rev. B* **36**, 8343 (1987).
- [106] B. Deissler, E. Lucioni, M. Modugno, G. Roati, L. Tanzi, M. Zaccanti, M. Inguscio, and G. Modugno, Correlation function of weakly interacting bosons in a disordered lattice, *New J. Phys.* **13**, 023020 (2011).
- [107] T. G. Kiely and E. J. Mueller, Superfluidity in the one-dimensional Bose-Hubbard model, *Phys. Rev. B* **105**, 134502 (2022).
- [108] T. D. Kühner, S. R. White, and H. Monien, One-dimensional Bose-Hubbard model with nearest-neighbor interaction, *Phys. Rev. B* **61**, 12474 (2000).
- [109] M.-C. Cha and J.-G. Shin, Two peaks in the momentum distribution of bosons in a weakly frustrated two-leg optical ladder, *Phys. Rev. A* **83**, 055602 (2011).